Maintenance of cell wall remodeling and vesicle production are connected in *Mycobacterium tuberculosis*

Vivian Salgueiro[1]*, Jorge Bertol[2]*, Claude Gutierrez[3], Ainhoa Palacios[4], Laia Pasquina-Lemonche[5], Akbar Espalliat[6], Laura Lerma[1], Brian Weinrick[7], Jose L. Lavin[8], Felix Elortza[4], Mikel Azkalgorta[4], Alicia Prieto[9], Pilar Buendía-Nacarino[10], José L. Luque-García[10], Olivier Neyrolles[3], Felipe Cava[6], Jamie K. Hobbs[5], Joaquín Sanz[2#] and Rafael Prados-Rosales[1#]

[1]Department of Preventive Medicine and Public Health and Microbiology, Universidad Autónoma de Madrid, Madrid, Spain;[2]Institute for Bio-computation and Physics of Complex Systems BIFI, Department of Theoretical Physics, University of Zaragoza, Zaragoza, Spain; [3]Institut de Pharmacologie et de Biologie Structurale, IPBS, Université de Toulouse, CNRS, UPS, Toulouse, France; [4]CIC bioGUNE, , Basque Research and Technology Alliance (BRTA), Bizkaia Science and Technology Park, Derio, Spain; [5]Department of Physics and Astronomy, University of Sheffield, Sheffield, UK; [6]Department of Molecular Biology and Laboratory for Molecular Infection Medicine Sweden, Umeå Centre for Microbial Research, SciLifeLab, Umeå University, Umeå, Sweden; [7]Trudeau Institute, Saranac Lake, NY, USA; [8]Bioinformatics Unit, Neiker-Tecnalia, Derio, Spain; [9]Department of Microbial & Plan Biotechnology, Centro de Investigaciones Biológicas Margarita Salas, Spanish National Research Council (CSIC),Madrid, Spain; [10]Department of Analytical Chemistry, Universidad Complutense de Madrid, Madrid, Spain.

Key words: extracellular vesicles, *Mycobacterium tuberculosis*, vesiculogenesis, peptidoglycan, membrane, permeability.

#To whom correspondence should be addressed:

Dr. Rafael Prados-Rosales– rafael.prados@uam.es

Dr. Joaquín Sanz- jsanz@bifi.es

***Equal contribution**

Running title: *Mycobacterium* vesicle biogenesis mechanism.

Abstract

Pathogenic and nonpathogenic mycobacteria secrete extracellular vesicles (EVs) under various conditions. EVs produced by *Mycobacterium tuberculosis* (*Mtb*) have raised significant interest for their potential in cell communication, nutrient acquisition, and immune evasion. However, the relevance of vesicle secretion during tuberculosis infection remains unknown due to the limited understanding of mycobacterial vesicle biogenesis. We have previously shown that a transposon mutant in the LCP-related gene *virR* (*virR*^{mut}) manifested a strong attenuated phenotype during experimental macrophage and murine infections, concomitant to enhanced vesicle release. In this study, we aimed to understand the role of VirR in the vesicle production process in *Mtb*. We employ genetic, transcriptional, proteomics, ultrastructural and biochemical methods to investigate the underlying processes explaining the enhanced vesiculogenesis phenomenon observed in the *virR* mutant. Our results establish that VirR is critical to sustain proper cell permeability via regulation of cell envelope remodeling possibly through the interaction with similar cell envelope proteins, which control the link between peptidoglycan and arabinogalactan. These findings advance our understanding of mycobacterial extracellular vesicle biogenesis and suggest that these set of proteins could be attractive targets for therapeutic intervention.

Introduction

Mycobacterium tuberculosis (*Mtb*) is one of the most successful human pathogens with the capacity to persist within the host establishing long-lasting infections. *Mtb* possesses multiple highly evolved mechanisms to manipulate host cellular machinery and evade the host immune system. Similar to other intracellular pathogens, *Mtb* releases proteins and lipids, that interfere with host cellular processes, via canonical or specialized secretion systems (Majlessi et al., 2015). How mycobacteria confined within phagosomes delivers virulence factors to other cellular compartments and/or into the extracellular milieu to affect the physiology of neighboring cells is currently a matter of investigation. Understanding the physiology of this phenomenon during the infection process might be critical to develop alternative therapies against tuberculosis (TB).

Like most forms of life, *Mtb* uses an alternative antigen release process based on extracellular vesicles (EVs) (R Prados-Rosales et al., 2011). Mycobacterial EVs (MEVs) are membrane walled spheres of 60-300 nm in diameter, released by live bacteria *in vitro* and *in vivo*. MEVs contain iron scavenging molecules, immunologically active complex lipids and lipoproteins, and classical virulence factors such as the *Mycobacterium ulcerans* toxin mycolactone (Lee et al., 2015; Marsollier et al., 2007; Prados-Rosales et al., 2014b; R Prados-Rosales et al., 2011). Several studies have clearly established a role of MEVs in immunomodulation and shown that MEVs deliver factors that impair macrophage effector functions, inhibit T cell activation, and modify the response of host cells to infection (Athman et al., 2017, 2015; Prados-Rosales et al., 2014b, 2014a; R Prados-Rosales et al., 2011; Rath et al., 2013). MEVs have also shown potential as biomarkers of *Mtb* infection (Schirmer et al., 2022; Ziegenbalg et al., 2013). Although the importance of MEVs has been recognized, hardly anything is known regarding both how such vesicles are exported across the mycobacterial cell wall and the molecular mechanisms underlying vesicle formation in mycobacteria. To date, several modulators of MEVs have been described. Our group identified two conditions leading to stimulation of vesicle production, namely: iron starvation (Prados-Rosales et al., 2014b) and the deletion of *virR* (Rv0431, vesiculogenesis and immune response Regulator) (Rath et al., 2013). In addition, it was shown that the Pst/SenX3-RegX3 signal transduction system regulates MEVs production independent from VirR (White et al., 2018), suggesting an alternative mechanism of vesicle production. We have recently demonstrated that both iron starvation and deletion of VirR in *Mtb*, two hypervesiculating conditions, trigger the induction of the isoniazid-induced gene operon *iniBAC* (Gupta et al., 2023). We determined that both IniA and IniC are dynamin-like proteins (DLP) presumably assisting MEV release through the fusion of the cell

membrane (Gupta et al., 2023; Wang et al., 2019). Understanding how defects in VirR lead to hypervesiculation through DLPs is important to provide mechanistic explanation for the vesiculation process in mycobacteria.

Several lines of evidence support the notion that VirR might be involved in maintaining cell wall integrity: (i) First, sequence analysis of the VirR protein indicates that it contains a conserved LytR_C domain (**Fig S1**), which is usually found in combination with another domain named LytR-Cps2A-Psr (LCP), and proteins carrying both domains have been associated with the remodeling of the cell wall in Gram-positive bacteria (Hubscher et al., 2008). *Mtb* has six genes encoding for LCP proteins, three with both LCP and LytR_C domains (Rv3267, Rv3484 and Rv0822), two with a solo LytR_C domain (VirR and Rv2700) and one protein with a solo LCP domain (Rv3840) (**Fig S1**). The LCP family includes enzymes that transfer glycopolymers from membrane-linked precursors to peptidoglycan (PG) or cell envelope proteins and are central to cell envelope integrity (Kawai et al., 2011). In mycobacteria its was demonstrated that some members of the (LCP) family of proteins are responsible for the linkage between arabinogalactan (AG) and PG (Grzegorzewicz et al., 2016; Harrison et al., 2016). Rv3267, Rv3484 and Rv0822 appear to have overlapping functions in cell wall assembly, Rv3267 being the primary ligase (Grzegorzewicz et al., 2016). Interestingly, while knocking down the gene encoding for the main AG-PG ligase (cg0847, *lcpA*) in *Corynebacterium glutamicum* leads to the release of outer membrane material to the extracellular medium (Baumgart et al., 2016), this phenotype is not observed in any knockout strain in the *Mtb* orthologs (Grzegorzewicz et al., 2016), probably reflecting the ability of the mutants to negatively regulate the biosynthesis of cell wall constituents in response to a decrease in ligase activity; (ii) Second, we and others have determined the increased susceptibility of the transposon *virR* mutant (*virR*^{mut}) with respect to the WT (Ballister et al., 2019; Rath et al., 2013), and the mutant in the *virR* ortholog, Rv2700 (cell envelope integrity, *cei*) to cell wall targeting drugs such as meropenem (Ballister et al., 2019). Based on these results, we hypothesize that LytR_C solo domain proteins including VirR and Cei Rv2700 have critical roles in the maintenance of cell wall homeostasis and their absence provokes cell wall alterations leading to enhanced vesiculation.

In this work we show that the absence of VirR leads to ultrastructural changes in the cell envelope as observed by cryo-electron microscopy (cryo-EM). These changes are compatible with enhanced permeability and an enlargement of the PG layer, as measured by high resolution atomic force microscopy (AFM). We demonstrate that VirR interacts with canonical LCP proteins and propose a model for such interaction. These results indicate that VirR is a central scaffold at the cell envelope

remodeling process assisting the PG-AG linking process and that this function is important for vesicle production in *Mtb*.

Results

High EV production linked to the lack of VirR is associated with an altered cell envelope in *Mtb* in the absence of cell lysis. While Gram-negative bacteria can release outer membrane vesicles directly into the extracellular environment from their outermost compartment, Gram-positive bacteria and mycobacteria have thick cell envelopes surrounding the cytoplasmic membrane that acts as a permeability barrier. The mycobacterial cell envelope is composed of PG covalently linked to AG, which in turn is decorated with exceptionally long-chain mycolic acids (MA). These MA, together with intercalating glycolipids, form the unique mycobacterial outer membrane (OM) (Kalscheuer et al., 2019). Previous analysis of mycobacterial vesicle associated lipids showed predominantly polar lipids, consistent with the cytoplasmic membrane being the likely origin of the vesicles (R Prados-Rosales et al., 2011). This is also true in EV produced by Fe-limited *Mtb* whose lipid content consists mainly of polar lipids and the lipidic siderophore, mycobactin (Prados-Rosales et al., 2014b). Given that these vesicles must traffic from their point of origin in the plasma membrane through the cell envelope, we hypothesized that local remodeling of the cell envelope is necessary for EV release, and that this process may be exacerbated in a *virR* mutant ($virR^{mut}$). To test this, we examined the cell envelope structure of $virR^{mut}$ grown in minimal medium (MM), as well as wild type (WT) and $virR^{mut}$ complemented ($virR^{mut}$-C) strains (Rath et al., 2013) (**Fig 1**). Using cryo-EM on whole cells, which allows the study of mycobacterial cell surface-associated compartments in a close-to-native state (Sani et al., 2010), we could easily discern three layers comprising the mycobacterial cell envelope: i) the outer membrane (OM); ii) an intermediate layer composed of two sublayers (L1 and L2, previously assigned to the mycolate-PG-AG (mAGP) network (Sani et al., 2010)); and iii) the cytoplasmic membrane (CM) (**Fig 1**). We observed a significant increase in the thickness of the overall cell envelope (OM-CM) in the $virR^{mut}$ strain compared to the WT. This difference was largely explained by the expansion of the CM-L1 layer, which appeared also more granulated, suggesting cell wall alterations closer to the cell membrane and indicating aberrant production of either AG, PG or both. Complementation with a functional copy of *virR* restored normal cell envelope structure (**Fig 1A-C**).

In Gram-negative bacteria increased vesiculation has been observed in conditions associated with either loss or maintenance of periplasm integrity (McMillan and Kuehn, 2021). Moreover, a novel mechanism of vesicle production common to both Gram-negative and Gram-positive bacteria has recently been described, in which a cell explosion phenomenon driven by bacteriophages leads to the formation of EVs in culture when bacteria are under genotoxic stress (Nagakubo et al., 2021). Consequently, we tested whether the enhanced vesiculation described in *virR*^{mut} (Rath et al., 2013) could be linked to cell lysis events. To do this, we analyzed the presence of cytoplasmic IdeR, a transcription factor which is not present in EVs and is not detected in secreted proteins preparations, in culture supernatants of *Mtb* strains, assuming that its detection could be linked to a loss of envelope integrity (Gupta et al., 2023). We first confirmed that the *virR*^{mut} strain manifested an enhanced vesiculation by measuring EVs using nanoparticle tracking analysis (NTA) (**Fig S2A**). We did not detect differences in size distribution of isolated EVs between strains. The same supernatants and cell lysates were used to detect the presence of IdeR by immunoblot using a specific polyclonal antibody (Pandey and Rodriguez, 2014). As a control for normal release of an extracellular protein, we used a monoclonal antibody against Ag85b (Prados-Rosales et al., 2017). We could not detect IdeR in the supernatant of any of the strains, indicating that defects of *virR* do not lead to cell lysis (**Fig S2B**). Taken together, the observed changes in the cell envelope of high EV producing bacteria suggest that cell envelope alterations in response to lack of VirR and increased membrane vesicle biogenesis may be connected in *Mtb*.

The absence of LytR_C solo domain proteins in *Mtb* leads to enhanced cell envelope permeability concomitant to hypervesiculation. The collective cryoEM observations that indicated an enlargement of the compartment next to the cell membrane may be linked to a more permeable cell envelope. Supporting this notion is the recent finding that *virR*^{mut} or the mutant in the *virR* ortholog *cei* (Rv2700) manifest an enhanced uptake of ethidium bromide (EtBr) relative to WT strain (Ballister et al., 2019). We could reproduce these results and add that *virR*^{mut}-C strain restores the permeability levels of the WT strain (**Fig 2A**). This enhanced permeability was concomitant to an increased sensitivity to different antitubercular drugs, including meropenem and vancomycin (Ballister et al., 2019). In agreement with these results, we could measure a significantly enhanced sensitivity of *virR*^{mut} to the PG-targeting drug vancomycin relative to WT and *virR*^{mut}-C strains (**Fig 2B**). Interestingly, the magnitude of the sensitivity to cell wall targeting drugs was either moderate (ethambutol) or absent (isoniazid) in *virR*^{mut} (Ballister et al., 2019). Furthermore, we

observed enhanced incorporation of fluorescent D-amino acids (FDAAs) in *virR*^{mut} relative to the WT strain in both MM and 7H9 media (**Fig 2C**), again suggesting increased permeability, altered PG turnover or both.

We then tested whether the enhanced permeability and vesiculation of *virR*^{mut} are also connected in an *Mtb* mutant lacking *cei* (Ballister et al., 2019). To do this, we generated *cei* conditional mutants using the CRISPR interference (CRISPRi) technology (Rock et al., 2017). Further, we also generated *virR* CRISPRi conditional mutants to properly compare both strains (**Fig 2D**). When these strains were cultured in the presence of anhydrotetracycline (ATc) to induce the transcriptional silencing of target genes, we could measure enhanced vesiculation by analyzing vesicle concentration in the supernatant by NTA (**Fig 2E**), relative to strains cultured in the absence of ATc. Overall, these results validate the enhanced permeability phenotype of *Mtb* mutants in the LytR_C solo domain proteins VirR and Cei and establish that this subfamily of proteins participates in the regulation of vesicle production in *Mtb*. Moreover, the higher susceptibility to PG-cross-linking inhibitors in both mutants and the enhanced incorporation of FDAAs in the *virR* mutant strain suggests defects in PG remodeling.

Transcriptional profiling of *virR*^{mut} showcases systemic alterations in cell wall architecture and metabolism. To identify VirR-dependent mediators of vesicle production, we carried out a transcriptional profiling of *virR*^{mut} and compared it to that of WT strain. Previous efforts to define the transcriptional profile of *virR*^{mut} showed no significant differences compared to WT (Rath et al., 2013). However, those experiments were carried out with bacteria grown in rich 7H9 medium, while here, we use a defined high-Fe minimal medium (MM), which is typically used for vesiculation experiments (R Prados-Rosales et al., 2011). We extracted RNA from four independent cultures (average optical densities (OD) of 0.4 and 0.38 for WT and *virR*^{mut}, respectively) one day before vesicle isolation and conducted RNA-seq. Of these, N=3 and N=4 libraries of WT and *virR*^{mut} passed QC (**Fig 3A**). Principal component analysis (PCA) was then performed on the transcriptomic data, after filtering out lowly expressed genes, as well as genes containing outlier observations (N=4004 genes tested), and revealed significant differences between strains, aligned with the first principal component (**Fig 3B**, one-tailed Mann-Whitney test p=2.86e-02), explaining as much as 78.27% of total gene expression variance. We then conducted differential expression analysis to find 1663 genes differentially expressed in *virR*^{mut} compared to WT (**Fig 3C**, Benjamini-Hochberg FDR<0.05), which represent 41.5% of all genes tested.

Next, we looked for gene ontologies enriched among these VirR-dependent genes, stratified by the direction of the effects (750 up-regulated, and 913 down-regulated in *virR*^{mut} relative to WT). The enrichment analyses highlighted five main groups of biological processes and cell compartment ontologies that appeared altered in *virR*^{mut} with respect to WT (**Fig 3D**). First, among genes that were expressed at lower levels in *virR*^{mut}, we found enrichments terms related to several stress associated with the intra-phagosomal environment (Schnappinger et al., 2003), such as response to hypoxia (FDR=1.14e-06), heat (FDR = 4.24 e-03) or oxidative stress (response to reactive oxygen species: FDR=9.00e-02), suggesting that responses to host-induced stress are compromised in the mutant, as it is also suggested by the enrichment of responses to host immune response (FDR=2.00 e-02). Furthermore, the mutant strain showed a reduction in transcripts related to the protein secretion term (FDR=2.51e-04), and, specifically, protein secretion by the type VII secretion system (FDR=1.15 e-04). Contributing to this enrichment, we found that both components of the key antigen-dimer ESAT-6/Cfp10, (Rv3875 and Rv3874, respectively), were significantly downregulated in the mutant strain (log2FC =-0.15, FDR=1.94 e-02 for Rv3875, and log2FC= -0.16, FDR = 2.25 e-02 for Rv3874).

Second, we found terms related to lipid metabolism and transport: (e.g. fatty acid biosynthetic process: FDR=4.92e-02; steroid metabolism, FDR=4.24e-03) enriched among downregulated genes in *virR*^{mut}, suggesting that the regulation of both anabolic and catabolic pathways of lipids, key for bacterial survival and pathogenesis upon infection (Ghazaei, 2018), are partially VirR-dependent. However, not every lipid-related pathway appeared downregulated in the mutant strain, since PDIM biosynthesis genes were predominantly up-regulated in the mutant (DIM/DIP cell wall layer assembly enrichment FDR=3.60e-02, and phenolic phtiocerol biosynthetic process FDR=3.60e-02).

The third group of enrichments included terms related to global regulation of gene expression, mostly enriched among downregulated genes in *virR*^{mut} (positive regulation of gene expression FDR=1.82 e-02, positive regulation of transcription, DNA templated FDR=4.92 e-02), suggesting a global alteration of the transcriptional landscape. The remaining two groups of ontologies included terms related to energy-production metabolism and post-transcriptional regulatory processes and compartments. Among these terms, we found evidence for an enrichment of genes encoding ribosome-located proteins (large ribosomal subunit, FDR= 3.60e-02) among genes up-regulated in *virR*^{mut}, which suggests the involvement of relevant VirR-dependent post-transcriptional regulatory processes impacting protein biosynthesis in the mutant. Similarly, enrichments of further key metabolic pathways beyond lipids

metabolic routes included terms enriched among genes down-regulated in *virR*^{mut}, such as electron transport chain, (FDR=9.15 e-03), and ATP biosynthetic process (FDR=1.36 e-02), as well as terms enriched among upregulated genes in the mutant such as NADH dehydrogenase activity, (FDR=1.53 e-02). All together, these results combined with the differences concerning lipid metabolism discussed above, suggest a global remodeling of metabolic networks in *virR*^{mut}.

virR* regulates the protein content of EVs in *Mtb. To capture the impact of transcriptional adaptation to the proteome and the degree of divergence between transcriptional shifts and proteins changes of *Mtb* in the absence of *virR*, we next performed label-free peptide mass spectrometry (LF-MS) of whole cell lysates (WCLs) of *virR*^{mut} and WT strains. Additionally, we isolated EVs from axenic cultures and obtained their proteomic composition to examine for potential VirR-dependent differences in protein cargo that may alter the functionality of EVs (**Fig 4A**). As a result, we obtained proteomic profiles across strains and cell compartments for a total of N=934 proteins. Upon PCA analysis of the proteomic data (**Fig 4B**), we found that the first principal component (PC1), explaining 36.8% of total variance, separated samples from WCLs and EVs regardless of the strain (PC1 differs across cell compartments: one-tailed Mann Whitney t test p=1.08e-03), while the second PC (PC2) (21.3% of total variance explained) captured strain effects on the proteomic footprint only among EVs (one-tailed Mann Whitney t test for PC2 differences between *virR*^{mut} EVs and the rest: p=4.55 e-03). These results suggest that differences in protein abundances between EVs and WCLs are larger than differences found between strains, and that, concerning the differences across strains, these are comparatively more important in EVs. Next, we conducted differential protein expression analyses to find 15 upregulated and 4 downregulated proteins between WT and *virR*^{mut} strains in WCLs, at FDR=5%, which represents 2% of the total of proteins under analyses (**Fig 4C, right bar**). Despite the scarcity of significant differences in expression across strains in WCLs, some of the proteins most differentially expressed in *virR*^{mut} are involved in key processes for bacterial survival and virulence, including key metabolic enzymes such as the Acetyl-coenzyme A synthetase AcsA (logFC = -3.78, FDR = 4.40 e-03), as well as FprA, (logFC= -2.77, FDR=1.55 e-02), involved in the reduction of NADP+ into NADPH, both downregulated in *virR*^{mut}.

Conversely to the WCL dataset, we did find larger differences in protein expression across strains in EVs, with 187 proteins more abundant and 166 less abundant in *virR*^{mut} EVs than that of WT (**Fig 4C, left bar**). This represents 37.8% of all proteins tested, a value largely comparable to the percentage of differentially

expressed genes identified in the RNA-seq data. Regarding downregulated EV proteins in *virR*^{mut} we observed robust enrichments in ontology terms related with protein biosynthesis, including translation (FDR=2.09 e-28), ribosome (FDR=3.01 e-37), and ribosome assembly (FDR=6.71 e-04), indicating that EVs from the *virR*^{mut} are ribosome-depleted. Consistent with these results 42 ribosomal proteins were found to be less abundant in the *virR*^{mut} strain relative to WT (**Fig S3**). Interestingly, these results contrast with the higher mRNA levels found for genes associated with the ribosomal compartment in the RNA-seq data obtained from WCLs (**Fig 3D**, **right panel**), suggesting that the depletion of ribosomal content found in the vesicles is the result of post-transcriptional regulatory events. Furthermore, we found that the two bacterioferritin proteins BfrA (log2FC=-3.19, FDR=3.42 e-04) and BfrB (log2FC=-2.47, FDR=9.70 e-05), were simultaneously less abundant in *virR*^{mut}, (**Fig 4E**), together contributing to the enrichment of the ontology term ferroxidase activity (FDR=8.30 e-02) (**Fig 4D**). This result is suggestive of a possible defect of *virR*^{mut} EVs in iron sequestration (Mohammadzadeh et al., 2021; Prados-Rosales et al., 2014b). We also found differences in metabolic pathways associated to the EV content, including enzymes involved in metabolism of nucleotides (FDR=9.63e-02 (up), (FDR=8.30e-02 (down), cellular amino acids ((FDR=6.26e-04 (up), FDR=1.41e-02 (down)) as well as carbohydrates (glycogen FDR=9.63e-02 (up), oligosaccharides FDR=8.30e-02 (down)). The simultaneous enrichments of these metabolic pathways observed both among upregulated and downregulated vesicular proteins (**Fig S4**), indicates a complex, VirR-dependent, rewiring of metabolic routes in the vesicles from the mutant strain.

Further, proteins upregulated in *virR*^{mut} EVs were enriched in terms related to mycolic acid metabolism (FDR=1.10 e-03), and peptidoglycan-based cell-wall biogenesis (FDR=1.44 e-02). Proteins such as InhA (logFC=3.65 FDR=6.10 e-05), and KasB (logFC=1.78 FDR=1.22 e-02), involved in mycolic acid synthesis were also upregulated in *virR*^{mut} (**Fig 4F**). The upregulation of these proteins, along with the enrichments at the transcriptional level of DIM/DIP biosynthetic pathways (upregulated in *virR*^{mut}), as well as steroid catabolic routes (down-regulated), suggests a shift in the control of the pool of propionyl-CoA, both at the level of its production, -as a byproduct of the catabolism of methyl-branched lipids, odd-chain-length fatty acids as well as cholesterol- and its detoxification by the bacterium through different routes, such as the methylmalonyl pathway, the glyoxylate cycle and the methylcitrate cycles (Lee et al., 2013). To shed light on these changes at the metabolic level, we conducted a metabolic profiling to quantify the concentration of metabolites that are central in these different detoxification routes including propionyl-CoA: acetyl-CoA, pyruvate,

methylcitrate, and methylmalonyl-CoA (**Fig 4G, left bottom panel**). Only methylmalonyl-CoA was found to be significantly repressed in *virR*^{mut} (p=0.028). This result, along with the trend towards increased protein, and especially gene expression that is observed for genes involved in the biosynthesis of PDIMs from methylmalonyl (including phenolpthiocerol synthesis type-I polyketide synthases A-E, (ppsA-E), fatty-acid-CoA synthetases fadD26 and fadD28, among others, **Fig 4G**), suggests that the methylmalonyl pool is depleted in the mutant strain as a result of an increased activity of the PDIM biosynthetic pathway. Furthermore, the acetyl/propionyl-CoA carboxylase subunits Acc, appear repressed in *virR*^{mut} EVs, suggesting that the production of methylmalonyl Co-A from the degradation of propionyl CoA is inhibited within the vesicles of the mutant strain.

Taken together, the omics analyses align with the structural and functional differences observed in *virR*^{mut}. We reasoned that the increased expression of PDIMs biosynthetic genes and the reduced expression of genes related to protein synthesis may be triggered to compensate the enhanced permeability measured in *virR*^{mut}. In addition, this enhanced permeability leads to an increase in the release of EV, which seems to be depleted in ribosomes and iron storage proteins.

Cell envelope permeability is a major driver of MEV release. If enhanced cell permeability is a global consequence of *virR* disruption that leads to enhanced vesiculation, we hypothesized that other conditions either inducing or decreasing cell envelope permeability could lead to alterations in vesicle production in *Mtb*. To test this, we treated *Mtb* with sublethal concentrations of thioridazine (TRZ), a known enhancer of cell permeability (De Keijzer et al., 2016); and, alternatively, we cultured the bacillus with cholesterol as a sole carbon source, a condition which reduces mycobacterial cell permeability (Brzostek et al., 2009) (**Fig 5A**). Neither condition altered bacterial viability as measured by the absence of the release of the transcription factor IdeR, as an indication of cell lysis (**Fig S2C**). We then measured vesicle levels in culture supernatants and found that *Mtb* significantly releases more vesicles upon treatment with TRZ, and significantly reduces vesicle release in the presence of cholesterol as a sole carbon source (**Fig 5B**), as measured by dot blot after normalization to colony forming units (CFUs). These results strongly suggest that cell envelope permeability determines the magnitude of the vesiculation phenomenon in *Mtb*.

We next investigated whether common transcriptional features underpin the regulation of cell envelope permeability in the tested conditions. To do that, we compared the transcriptional response of *virR*^{mut} with that of available datasets including *Mtb* cultured in the presence of 0.01% of cholesterol as a sole carbon source

(Pawełczyk et al., 2021), and *Mtb* treated with 6 μg ml^{-1} of TRZ (Dutta et al., 2010). Experimentally, we retrieved the set of genes up and down-regulated in *Mtb* grown in cholesterol vs glucose-rich culture media (Brzostek et al., 2009), and interrogated whether those genes were enriched among the sets of differentially expressed genes in *virR*^{mut} vs WT reported in this study (**Fig 5C**). Interestingly, we found that those genes whose expression changed in the same direction in conditions associated with low, or high permeability, in both studies were mutually enriched, while the cross-comparisons between sets with opposite responses to low-permeability-associated treatments in both studies led to significant depletion statistics. These results validate the initial hypothesis according to which changes in permeability induced by these two treatments are linked to the activation of a common transcriptional program. The inspection of genes that are simultaneously upregulated in treatments associated with low permeability in both studies identified DosR as a putative regulator associated with the orchestration of this transcriptional footprint of low cell permeability. The two-component system DosS-DosR has a well-known role as a global regulator of the transition to dormancy, and its regulon is consistently upregulated in non-permeable dormant bacteria (Honaker et al., 2009). Interestingly, authors found that low-permeability bacteria cultured in a cholesterol medium, albeit featuring a regular growing phenotype, activated the DosR regulon, suggesting that cell wall remodeling leading to a decrease in permeability linked with the induction of DosR can be triggered independently to the transcriptional regulatory programs leading to growth arrest and dormancy in *Mtb* (Pawełczyk et al., 2021). Importantly, the integration of the genes that are down-regulated in *virR*^{mut} validates this hypothesis (**Fig 5D** and **FigS5**), since 39 out of the 48 genes annotated in the DosR regulon are simultaneously up-regulated in conditions linked to low permeability in both studies.

A similar analytic approach for the comparison of the response of *virR*^{mut} and the response to the drug TRZ, a treatment well-known for inducing an increase in permeability in *Mtb*-treated cells (Dutta et al., 2010) (GSE16626), led to conceptually similar results, with genes simultaneously upregulated in both TRZ and *virR*^{mut} (OR=1.51, p=0.03), as well as genes simultaneously down-regulated (OR=1.48, p=0.03), being marginally enriched. Interestingly, among the 20 genes showing the largest, and most significant repression effects by both treatments (log2FC>0.5 & FDR<0.05 in both analyses), we found 6 genes whose functions are related with metal nutrients uptake, homeostasis and metabolism, such as genes encoding the bacterioferritin BrfB, rubredoxins RubA and RubB, metal homeostasis sensors CsoR (copper) and kmtR (nickel and cobalt), and the metal exporter CtpJ (**Fig 5E**). Taken together, these analyses highlight the transcriptional parallels between *virR*^{mut} and both

TRZ and cholesterol conditions, which strongly suggests the existence of a common transcriptional signature associated with the control of cell permeability.

The absence of VirR leads to an aberrant enlargement of PG in *Mtb*. To elucidate the specific molecular defects that explain the periplasm enlargement, the enhanced permeability, and the antibiotic sensitivity phenotypes, we performed a biochemical analysis of WT and *virR*^{mut} cell envelopes. First, we analyzed the total lipid profile by liquid chromatography-mass spectrometry (LC-MS) and observed significant differences in prevalent polar lipids linked to the cell membrane including, lysophosphatidic and phosphatidic acid, species of monoacylated and diacylated glycerol, phosphatidylethanolamines and phosphatidyl-myo-inositol mannoside (PIM) species, being more abundant in *virR*^{mut} relative to WT and complementing strain. (**Fig 6A**). To validate these results, we ran thin layer chromatography (TLC) analysis on the same lipid extracts and found that the mutant carries more phospholipids in the membrane including more $AcPIM_2$ and PE (**Fig 6B**). Moreover, we could not measure major differences in the level of mycolic acid species (**Fig 6C**), while significantly more PDIMs were detected in the mutant relative to the other strains (**Fig 6D**). This later result agrees with that of transcriptomics and proteomics analyses. When analyzing apolar lipids we also observed increased levels of free mycolic acids (FMA) and free fatty acids (FFA) upon *virR* deletion (**Fig 6E**). The enhanced release of these apolar lipids has also been documented in a *C. glutamicum* mutant in Cg0847 (Baumgart et al., 2016), a canonical LCP protein. Importantly, we could not detect any of these lipids in EVs from *virR*^{mut} (**Fig 6F**), while major polar phospholipids could be resolved in EVs from all strains (**Fig 6G**), as previously reported (R Prados-Rosales et al., 2011). This result indicates that *Mtb* releases free apolar lipids independently from membrane associated EVs.

Next, we performed a glycosyl composition analysis of isolated cell walls (including mycolyl-arabinogalactan-peptidoglycan complex) and determined that there were no significant differences between strains in AG content as well as in the ratio between arabinose and galactose (A/G) (**Fig 7A**). Similarly, no changes were observed in the galactan length as measured by the ratio between galactose (G) and rhamnose (R) G/R) (Justen et al., 2020). We noticed that the ratio between N-acetylglucosamine (NAGc) and rhamnose (R) (NAGc/R) was significantly higher in *virR*^{mut} relative to WT, suggesting an increase in PG content in this strain (**Fig 7A**). The validation of these results was performed independently by measuring the amount of diaminopimelic acid (DAP) in isolated cell walls, as a surrogate of PG content, and determined that *virR*^{mut} carries two times more PG than WT or complemented strains (**Fig 7B**). We next

obtained pure PG preparations of each strain and performed an analysis by atomic force microscopy (AFM) (**Fig 7C and Fig S6**). This technique has been recently used to investigate the nanometric features of isolated Gram-positive bacterial cell walls (Pasquina-Lemonche et al., 2020). Semi-automated analysis of liquid AFM images from mycobacterial isolated PG samples revealed that: (i) the absence of VirR leads to a significant reduction in PG pore diameter (down to 9.2 ± 0.6 nm) relative to WT (16 ± 3.3 nm) and complemented strains (10 ± 0.8 nm) (**Fig 7C, D and Fig S6**); (ii) the number of pores is significantly higher in *virR*^{mut} compared to WT and complemented strain (**Fig 7E and Fig S6**); (iii) manual analysis of AFM images in ambient conditions revealed that *virR*^{mut} PG is significantly thicker than that of the other strains of the study (**Fig 7F**). These results show for the first time the nanometric architecture of isolated PG in mycobacteria by AFM and suggest a role for VirR in regulating PG thickness and porosity. Strikingly, we found that the PG enlargement observed in the *virR*^{mut} correlated with increased susceptibility to the muramidase lysozyme (**Fig S7**), indicating modifications in PG remodeling in *virR*^{mut}. Collectively, although the structural changes at nanoscopic level of the peripheral areas of the cell observed by AFM leads to a more dense and thick structure harder to penetrate, the chemical changes in the peptidoglycan structure observed and biochemical assays suggest that changes associated with alterations in VirR-regulated PG remodeling makes the wall more permeable and support increased release of EV in *Mtb*.

VirR interacts with canonical LCP proteins. As mentioned above VirR is a LytR_C solo domain protein with no catalytic LCP domain. Other members of the LCP protein family like Rv3267 and Rv3287 are the main PG-AG ligases (Grzegorzewicz et al., 2016; Harrison et al., 2016) and also carry a LytR_C domain. We have previously shown that VirR interacts with itself (Rath et al., 2013). Consequently, we reasoned that if VirR contributed to PG-AG ligation it could do it via interaction with canonical LCP proteins through the LytR_C domain. Although VirR is one of the most abundant proteins found in tuberculin preparations (Prasad et al., 2013), we determined that it localizes at sites of nascent cell wall by fluorescence microscopy (**Fig S8**). Therefore, its location could initially allow for interactions with other cell surface proteins like LCP. Both recombinant VirR and the main AG-PG ligase Lcp1 (Rv3267) oligomerize in a blue-native PAGE gel (**Fig 8A**). This observation suggests that they interact with proteins sharing similar domain features. We next performed a flotation assay where we examined the behavior of VirR on an iodixanol gradient in the presence or absence of Lcp1. Using a specific antibody raised against VirR, we observed that the presence of Lcp1 displaces the relative location of VirR toward upper fractions of the gradient,

indicating a potential interaction of both proteins and the formation of higher molecular weight complexes (**Fig 8B**). To investigate the interaction of virR and Lcp1, along with other Lcp proteins, in a more physiological environment we used the bipartite splitGFP approach (Cabantous et al., 2013) (**Fig 8C and Fig S9**), which has been recently utilized to demonstrate the co-localization and interaction of the membrane-bound metal ATPase CtpC with the chaperon PacL1 (Boudehen et al., 2022). We first recapitulated the VirR self-interaction and added that such interaction implicates the LytR_C domain since no differences in fluorescence were measured between full and truncated versions of VirR (VirRsol) lacking the first 41 amino acids. As negative controls, we included interactions between VirR and the cell surface associated metal ATPase CtpC (**Fig 8C**). When testing interactions between VirR and other Lcp proteins (Rv0822c, Lcp1 (Rv3267) and Rv3284) we could not measure any GFP signal when full Lcp proteins were used in the assay. Conversely, a significant increase in fluorescence was measured for all combinations when truncated Lcp proteins including either the C-terminal domain or specifically the LytR_C domain were tested (**Fig 8C**). These results strongly suggest that VirR interacts with Lcp proteins and that these interactions occur via LytR_C terminal domains.

DISCUSSION

Our group reported *virR* as the first gene implicated in the biogenesis of EVs in *Mtb* ten years back (Rath et al., 2013). A transposon mutant in *virR* (*virR*^{mut}) overproduces MEVs and this provokes augmentation of cytokine responses in mouse and human macrophages. This mutant manifested an attenuated phenotype in experimental infections on macrophages and mice (Beaulieu et al., 2010; Rath et al., 2013). Such studies established that VirR has a role in virulence by negatively modulating the release of MEVs. These studies provided evidence that vesiculogenesis in *Mtb* is genetically regulated. Since then, conditions such as iron starvation (Prados-Rosales et al., 2014b) and other genes including *iniAC* (Gupta et al., 2023) and the Pst/SenX3-RegX3 signal transduction system (White et al., 2018) have been shown to contribute to the biogenesis of MEVs. Interestingly, VirR, a LytR_C solo domain protein (**Fig S1**), shares homology with Lcp proteins, which in *Mtb* are known to participate in the enzymatic connection between AG and PG (Grzegorzewicz et al., 2016; Harrison et al., 2016). This suggests VirR function might be linked to cell wall remodeling.

In this study, we investigated how VirR can control the magnitude of MEV release in *Mtb*. We did this by studying the underlying enhanced vesiculogenesis phenomenon observed in *virR*^{mut} using genetic, transcriptiomics, proteomics and ultrastructural and biochemical methods. It was clear from our cryo-EM studies that

virR^{mut} has an aberrant cell wall as the layer above the cell membrane was significantly larger than that of WT and complemented strains. The enlarged compartment showed higher granular texture, a feature that has been previously associated to PG precursors in unrelated Gram-positive bacteria (Zuber et al., 2006). This observation and previous studies showing the increased sensitivity of *VirR*^{mut} to vancomycin (Ballister et al., 2019) strongly suggested that the cell wall defect is connected to PG remodeling. The use of AFM on isolated PG confirmed this and showed for the first time the nanostructure of PG in *Mtb*, providing information on PG thickness, pore size and number of pores. AFM indicated that *virR*^{mut} PG is thicker, has significantly more pores of small size. Considering the pore sizes measured across strains (ranging from 9-16 nm), we initially ruled out the notion that EVs (which are spheres of 50-300 nm in diameter) are released through the peripheral cell wall. Therefore, *Mtb* must have an alternative mechanism to release EVs, possible during the division process where the PG is most fragile, presumably due to defects in crosslinking. These events were not possible to visualize in AFM given that PG fragments from all the strains were lacking the poles or clearly defined division sites but could be the subject of further studies in the future. However, we cannot exclude that MEV plasticity could allow for crossing the cell wall via PG pores.

A recent study showed that *Corynebacterium glutamicum* can produce and release different types of MVs through different routes, including mycomembrane blebbing or bubbling cell death, depending on the stress at which *C. glutamicum* is exposed (Nagakubo et al., 2021). In the present study, we have shown that *virR*^{mut} overproduces EVs under normal growing conditions in the absence of cell lysis, according to our assay which measured cytoplasmic leaking of the transcription factor IdeR. Overall, we show that EV production in *Mtb* under our growing conditions, is not linked to cell death. This fact largely excludes the bubbling cell death mechanism. Moreover, our lipidomic analysis now and before (Rafael Prados-Rosales et al., 2011) indicates the absence of mycomembrane lipids in isolated MEVs from all strains, ruling out that MEVs originate at the mycomembrane. These apparent disagreements with the *C. glutamicum* study (Nagakubo et al., 2021) might indicate that *Mtb* EV biogenesis may differ from that of *C glutamicum*, and other mycolic acid-containing bacteria with shorter fatty acids. Additional variables that may explain differences between studies is the growth media and the time at which vesicles are isolated (Gupta et al., 2023). Of note, *M. smegmatis* EVs were isolated at day 6 (Nagakubo et al., 2021), a time at which this fast-growing mycobacteria is already in stationary phase.

The transcriptional profile of *virR*^{mut} can provide a partial explanation for the attenuated phenotype of the mutant due to a downregulation of genes activated upon

stresses associated to the intraphagosomal environment. It is particularly interesting to observe the specific reduction in transcript levels of the two most important effectors of the esx-1 secretion system. On the other hand, genes involved in PDIM synthesis were upregulated. It is possible that the specific upregulation of PDIM synthesis in absence of *virR* is part of compensatory response to a reduced permeability. We were surprised to find no differences between protein profiles in whole cells between WT and *virR*^{mut} strains, despite difference in transcriptomics. A biological interpretation of these results would point to the existence of global compensatory mechanisms of post-transcriptional regulation used by the bacteria to partially recover comparable proteomic profiles in *virR*^{mut} to those observed in the WT.

Contrary to whole cell lysates, EV protein profiles between *virR*^{mut} and WT were largely different. In this context, it is accepted that certain proteins and lipids are enriched in bacterial EVs and that preferential inclusion of such antigens in MVs supports a specific vesicle biogenesis mechanism. In Gram positive bacteria and mycobacteria both membrane and cytosolic proteins are included in EVs since the origin of these structures is linked to the cell membrane (R Prados-Rosales et al., 2011) and, presumably, the incorporation of intracellular proteins may occur during the process of vesicle formation. We found a higher abundance of proteins related to PG and MA synthesis in *virR*^{mut} EVs relative to WT. Therefore, these two processes seem to contribute to EV biogenesis in *Mtb*. Additional data presented in this study, which includes ultrastructural and chemical analyses confirm this. Both PG and MA synthesis are complex processes, including a diverse set of genes. What parts of the biogenesis of these molecules are important for the formation of EVs is a matter of future investigations.

Another finding of the study is the connection between permeability and the magnitude of the vesiculation process in *Mtb*. We linked these two phenomena first, by measuring enhanced vesiculation and permeability in the same strain (*virR*^{mut}) and second, by modifying the permeability using chemical (via sublethal exposure to TRZ) and nutritional supplements (via providing cholesterol as sole carbon source) in WT *Mtb*. TRZ, a repurposed drug that belongs to the class of phenothiazines, is known to affect respiration in *Mtb* (Amaral et al., 1996). It is also assumed that TRZ can inhibit efflux pumps leading to an increased susceptibility to first line antitubercular drugs when tested in combination (De Knegt et al., 2014). This provides an explanation for the synergistic effects of such combinations. An independent explanation of such synergy may also come from the increased permeability, as it has been recently shown by a quantitative proteomics analysis of *Mtb* cells exposed to sublethal concentration of TRZ (De Keijzer et al., 2016). When we grew *Mtb* with cholesterol as a sole carbon

source, a condition that slows mycobacterial growth but also reduces cell permeability via cholesterol accumulation in the cell wall (Brzostek et al., 2009), we observed the opposite trend on MEV biogenesis. We consider this finding of high relevance since *Mtb* permeability is one the major concerns when developing potential antimycobacterial drugs. Nevertheless, bacterial cell permeability is a complex property that it is controlled by physiochemical, biological, and chemical processes such as stereochemistry, lipophilicity, saturation and unsaturation, flexibility, viscosity, fluidity, pressure, temperature and physiological conditions (Nagamani and Sastry, 2021). How these variables change to allow the release of MEVs is not known.

This study also proposes a model VirR function whereby VirR may work as a scaffold for canonical Lcp proteins, which in *Mtb* links PG to AG. Based on the demonstration that VirR interacts with canonical Lcp proteins, we believe that the absence of VirR deregulates the localization of canonical Lcp proteins. Although we cannot rule out the contribution of other phenomena including alteration of the PG molecule, VirR is a central scaffold in the cell wall remodeling process. Taking into consideration the fact that $VirR^{mut}$ is attenuated in virulence on preclinical models of infections and manifests an enhanced vesiculogenesis and permeability, VirR may represent a novel and interesting drug target. We envision that targeting VirR may not only make *Mtb* weaker and more permeable to other antitubercular drugs, but to stimulate the immune system, via MEVs, to fight infection.

MATERIALS AND METHODS

Bacterial Strains, media and growth conditions. *Mtb* H37Rv (ATCC) and derivative strains $virR^{mut}$ and $virR^{mut}$-*C* (complemented strain) (Rath et al., 2013) were used in this study. Bacteria were initially grown in Middlebrook 7H9 medium (7H9) supplemented with 10% (v/v) oleic acid-albumin-dextrose-catalase (OADC) enrichment (Becton Dickinson Microbiology Systems, Spark, MD, United States), 0.5% (v/v) glycerol and with Tyloxapol 0.05% (v/v; Sigma-Aldrich, Burlington, MA, United States) prior to inoculation in a minimal medium (MM) consisting of KH_2PO_4 1 g/l, Na_2HPO_4 2.5 g/l, asparagine 0.5 g/l, ferric ammonium citrate 50 mg/l, $CaCl_2$ 0.5 mg/l, $ZnSO_4$ 0.1 mg/l, without Tyloxapol 0.05% (v/v), containing 0.7% (v/v) glycerol, pH 7.0.

Mtb was also cultured in MM in the presence of sublethal concentrations of thirodazine (TRZ) of 6 μgml^{-1} as previously described. We determined that this concentration does not affect cell growth. *Mtb* was also cultured in MM with cholesterol as a sole carbon source as previously described (Brzostek et al., 2009).

Mtb expressing fluorescent VirR was generated by cloning VirR into pMV261-Venus using fast cloning approach (Li et al., 2011).

M. smegmatis mc^{2}155 (ATCC 700084) and recombinants derived from this strain were grown at 37°C in 7H9 medium (Difco) supplemented with 10% albumin-dextrose-catalase (ADC, Difco) and 0.05% Tween-80 (Sigma-Aldrich), or on complete 7H11 solid medium (Difco) supplemented with 10% OADC(Difco). When needed, streptomycin (25 µg ml^{-1}) was added to the culture media. *Escherichia coli* strains StellarTM (Takara bio, San Jose, CA, United States) were grown at 37°C in LB broth (Difco) or on L-agar plates (Difco) supplemented with streptomycin (25 µg ml^{-1}) when required.

***M. smegmatis* expression vectors for split GFP experiment.** Plasmids used for split GFP experiments were constructed by modifying the plasmid pGMCS-PpacL1-pacL1-Lk2-GFP11-ctpC(1-85)-Lk15-GFP(1-10) (Boudehen et al., 2022) (**Table S1**). Plasmids pGMCS, conferring resistance to streptomycin, are shuttle vectors, episomal in *E. coli* and integrative in mycobacteria through insertion at the attL5 mycobacteriophage insertion site in the glyV tRNA gene. Lk2 (LEGSGGGGSGGGS) and Lk15 (GPGLSGLGGGGGSLG) are flexible linkers separating the protein domains of interest from the last 11th b-sheet or the first ten b-sheets of GFP, respectively. First, the Zinc-inducible PpacL1 promoter was replaced by P1, a strong constitutive promoter from *M. smegmatis* (Ariyachaokun et al., 2020), resulting in pGMCS-P1-pacL1-Lk2-GFP11-ctpC(1-85)-Lk15-GFP(1-10). Second, the pacL1 (Rv3269) sequence was replaced by that of virR (encoding amino-acids 1 to 164) or virRsol (encoding amino-acids 42 to 164) by In-Fusion HD cloning (Takara). PCR fragments were amplified using appropriate primer pairs (**Table S1**) and Phusion High-Fidelity PCR Master Mix with GC Buffer (Thermo Scientific, Walthman, MA, United States). Linear fragments were purified on agarose gels and inserted into pGMCS backbone linearized by PCR amplification with appropriate primers, using the In-Fusion HD Cloning Kit (Takara), following the manufacturer's instructions. Finally, the ctpC sequence was replaced on the resulting plasmids by the virR or virRsol sequences, or that encoding either the C-terminal part or only the LytR_C domains of the Rv0822c, Rv3267 or Rv3484 proteins from *M. tuberculosis* H37Rv. Plasmids were constructed by transformation into *E. coli* Stellar recipient cells. All plasmids were verified by sequencing before introduction by electroporation into *M. smegmatis* mc²155 strain.

Generation of the CRISPR mutants. To generate the conditional CRISPR mutants we took advantage of the CRISPR interference (CRISPRi) technology (Rock et al., 2017).

Briefly, we designed sgRNA oligonucleotides containing the target Rv0431 (*virR*) and Rv2700 (*cei*) genes sequences (**Table S1**) located immediately upstream of the PAM sequence. The strengths of the PAM sequence were chosen following authors recommendation to get high and intermediate gene repression, 158.1 or 42.2-fold repression for *virR* and 145.2 and 47.3 for *cei*, respectively. The primers were annealed and ligated into the gel purified BsmBI-digested CRISPRi vector (plJR965 plasmid) followed by transformation of competent *Mtb* cells via electroporation. Transcriptional knockdown of genes were quantified by qRT-PCR; and protein levels were examined by immunoblot using specific antibodies raised against VirR (Rath et al., 2013) and Cei (Ballister et al., 2019) **.**

EV isolation and purification. *Mtb*-EV were prepared and purified as previously described. Briefly, the culture filtrate of 1 L cultures of *Mtb* grown in low iron MM without detergent for 14 days was processed for vesicle isolation by differential centrifugation. In parallel a 2 ml culture in MM supplemented with 0.05% Tyloxapol to disperse bacterial clumps was used to determine viability by plating culture dilutions onto 7H10 agar plates and enumerating colony forming unit (CFU) at the time of culture filtrate collection.

The membranous pellet containing vesicles obtained after ultracentrifugation of the culture filtrate at 100,000 × g for 2 h at 4°C, was resuspended in 1 ml sterile phosphate-buffered saline (PBS) and overlaid with a series of Optiprep (Sigma-Aldrich) gradient layers with concentrations ranging from 30% to 5% (w/v). The gradients were centrifuged at 100,000 × g for 16 h. At the end 1 ml fractions were removed from the top, diluted to 20 ml with PBS and purified vesicles recovered by sedimentation at 100,000 × g for 1 h. Vesicle pellets were suspended in PBS before analysis. Protein concentration was measured by Bradford assay (Bio Rad, Hercules, CA, United States) according to manufacturer instructions. For all conditions test from which EVs were isolated, normalization was performed by referring EVs concentration to colony forming units (CFUs).

Nano particle tracking analysis (NTA). NTA was conducted using ZetaView (Particle Metrix, Winning am Ammersee, Germany). Instrument calibration was performed prior to EV analysis using 102 nm polystyrene beads (Thermo Fisher Scientific), according to manufacturer instructions. Measurements were performed using a 405 nm 68 mW laser and CMOS camera by scanning 11 cell positions and capturing 60 frames per position at 25□C with camera sensitivity 85, shutter speed 100, autofocus and automatic scattering intensity. Samples were diluted in pre-filtered PBS to

approximately 106-107 particles·ml^{-1} in Millipore DI water. Analysis was performed using ZetaView Software version 8.05.12 SP1 with a minimum brightness of 30, maximum brightness of 255, minimum area of 5, maximum area of 1000, and s minimum trace length 15. Triplicate videos of each sample were taken in light scatter mode. Particle size and concentration were analyzed using the built-in EMV protocol and plotted using Prism software, version 8.0.1 (GraphPad Inc., San Diego, CA, United States).

Electron-Microscopy. Cells were fixed with 2% glutaraldehyde in 0.1 M cacodylate at room temperature for 24 h, and then incubated overnight in 4% formaldehyde, 1% glutaraldehyde, and 0.1% PBS. For scanning microscopy, samples were then dehydrated through a graded series of ethanol solutions before critical-point drying using liquid carbon dioxide in a Toumisis Samdri 795 device and sputter-coating with gold-palladium in a Denton Vacuum Desk-2 device. Samples were examined in a Zeiss Supra Field Emission Scanning Electron Microscope (Carl Zeiss Microscopy, LLC, North America), using an accelerating voltage of 5 KV.

For Cryo-EM, grids were prepared following standard procedures and observed at liquid nitrogen temperatures in a JEM-2200FS/CR transmission electron microscope (JEOL Europe, Croissy-sur-Seine, France) operated at 200 kV. An in-column omega energy filter helped to record images with improved signal/noise ratio by zero-loss filtering. The energy selecting slit width was set at 9 eV. Digital images were recorded on an UltraScan4000 CCD camera under low-dose conditions at a magnification of 55,058 obtaining a final pixel size of 2.7 Å/pixel.

Density profiles were calculated along rectangular selections with the ImageJ software (NIH, Bethesda, MD, United States). The number of cells analyzed varied from n = 20 (WT), n = 15 (*virR*^{mut}) and n = 23 (*virR*^{mut}-C). The comparisons extracted from this data is statistically relevant with t test with Welch's correction performed. For each cell three representative measurements were obtained. Mean and standard error was then calculated for measurements pooled for each strain.

Western Dot blot. Two µl of EV isolates and two-fold serial dilutions were spotted onto a nitrocellulose membrane (Abcam, Cambridge, United Kingdom) and process for dot blot using anti-EV polyclonal murine serum (Prados-Rosales et al., 2014a) as primary antibody and goat anti-mouse-HRP conjugated as secondary antibody and ECL prime Western Blotting Detection chemiluminescent substrate (GE Healthcare, Chicago, IL, United States). The signal was visualized in a Chemidoc MP imaging system (Bio Rad)s).

RNA sequencing. *Mtb* strains were grown in MM supplemented with 0.05% Tyloxapol at 37ºC until they reached an OD595nm of 0.3 and harvested by centrifugation. The cell pellets were resuspended in 1 ml Qiagen RNA protect reagent (Qiagen, Venlo, Netherlands) and incubated for 24 h at room temperature. Cells were disrupted by mechanical lysis in a FastPrep-24 instrument (MP Biomedicals, Santa Ana, CA, United States) in Lysing Matrix B tubes and RNA was purified with the Direct-zol RNA miniprep kit (Zymo Research, Irvine, CA, United States). The quantity and quality of the RNAs were evaluated using Qubit RNA HS Assay Kit (Thermo Fisher Scientific) and Agilent RNA 6000 Nano Chips (Agilent Technologies, Santa Clara, CA, United States), respectively. Sequencing libraries were prepared using the Ribo-Zero rRNA Removal Kit (Gram-positive Bacteria) (Illumina Inc., San Diego, CA, United Stated) and the TruSeqStranded mRNA library prep kit (Illumina Inc), following the Ribo-Zero rRNA Removal kit Reference guide and the "TruSeqStranded mRNA Sample Preparation Guide. Briefly, starting from 1 µg of total RNA, bacterial rRNA was removed and the remaining RNA was cleaned up using AgencourtRNAClean XP beads (Beckman Coulter). Purified RNA was fragmented and primed for cDNA synthesis. cDNA first strand was synthesized with SuperScript-II Reverse Transcriptase (Thermo Fisher Scientific) for 10 min at 25°C, 15 min at 42°C, 15 min at 70°C and pause at 4°C. cDNA second strand was synthesized with Illumina reagents at 16°C for 1 hr. Then, A-tailing and adaptor ligation were performed. Libraries enrichment was achieved by PCR (30 sec at 98°C; 15 cycles of 10 sec at 98°C, 30 sec at 60°C, 30 sec at 72°C; 5 min at 72°C and pause at 4°C). Afterwards, libraries were visualized on an Agilent 2100 Bioanalyzer using Agilent High Sensitivity DNA kit (Agilent Technologies) and quantified using Qubit dsDNA HS DNA Kit (Thermo Fisher Scientific). Library sequencing was carried out on an Illumina HiSeq2500 sequencer with 50 nucleotides single end reads and at least 20 million reads per individual library were obtained.

RNA-sequencing data analysis. Quality Control of sequenced samples was performed by FASTQC software (http://www.bioinformatics.babraham.ac.uk/projects/fastqc/). Reads were mapped against the *M. tuberculosis* H37Rv strain (GCF_000195955.2_ASM19595v2) reference genome using Tophat (Trapnell et al., 2009) with --bowtie1 option, to align 50 bp reads. The resulting BAM alignment files for the samples were the input to Rsubread's (Liao et al., 2019) featureCounts function to generate a table of raw counts required for the Differential Expression (DE) analysis. Data preprocessing and differential expression analysis of the transcriptomic data was performed using DeSeq2 (Love et al., 2014).

Genes with a median of expression lower than 1 CPM, and genes containing outlier observations were filtered before statistical modeling, and the remaining N=4004 genes were used for differential expression analysis. P-values were corrected for multiple testing using the R package, implementing the Storey-Tibshirani FDR correction method (Storey et al., 2023). Genes with an FDR<0.05 were deemed as differentially expressed. Data were deposited at Gene expression Omnibus (GEO); GSE143996.

Label-free mass spectrometry analysis. Total cell proteins and MEV-associated proteins were submitted to LC-MS label-free analysis using a Synapt G2Si ESI Q-Mobility-TOF spectrometer (Waters) coupled online to a NanoAcquity nano-HPLC (Waters), equipped with a Waters BEH C18 nano-column (200mm x 75 um ID, 1.8um). Samples were incubated and digested following the filter-aided sample preparation (FASP) protocol (Wiśniewski et al., 2009) Trypsin was added to a trypsin:protein ratio of 1:50, and the mixture was incubated overnight at 37°C ,dried out in a RVC2 25 speedvac concentrator (Christ), and resuspended in 0.1% FA. Peptides were desalted and resuspended in 0.1% FA using C18 stage tips (Millipore). Digested samples (500 ng) were loaded onto the LC system and resolved using a 60 min gradient (5 to 60% ACN). Data was acquired in HDDA mode that enhances signal intensities using the ion mobility separation step. Protein identification and quantification were carried out using Progenesis LC-MS (version 2.0.5556.29015, Nonlinear Dynamics). One of the runs was used as the reference to which the precursor masses in all other samples were aligned to. Only features comprising charges of 2+ and 3+ were selected. The raw abundances of each feature were automatically normalized and logarithmized against the reference run. Samples were grouped in accordance with the comparison being performed, and an ANOVA analysis was performed. A peak list containing the information of all the features was generated and exported to the Mascot search engine (Matrix Science Ltd.). This file was searched against a Uniprot/Swissprot database, and the list of identified peptides was imported back to Progenesis LC-MS. Protein quantitation was performed based on the three most intense non-conflicting peptides (peptides occurring in only one protein), except for proteins with only two non-conflicting peptides.

Proteomics data analysis. Normalization and imputation of the proteomics data was done using the DEP package for R (Zhang et al., 2018). Normalization was done using the vsn method (Huber et al., 2002), which transforms data tackling heteroskedasticity. Imputation of missing values was performed using the bpca method (Oba et al., 2003), which leans on principal component analysis to impute missing values.

Data was analyzed according to a design where differences between strains (*virR*^{mut}-WT) were estimated independently within each cell compartment, (whole cell lysates or EVs). according to a nested design: Expression ~ Compartment + Strain:Compartment. Differential expression analysis of the proteomics data was performed using limma (Ritchie et al., 2015) and p-values were corrected for multiple testing according to the Storey-Tibshirani method using the R package qvalue (Storey et al., 2003). Proteins with an FDR<0.05 were selected as differentially expressed.

Gene ontology (GO) enrichments*.* Enrichment analyses of the sets of differentially expressed genes and proteins were performed in R using the terms of the Gene Ontology database for testing, version 11.02.2020. Gene sets corresponding to the biological process and cellular component ontologies between levels 4 to 6 (N=2245) were selected and filtered according to their size (minimum size =10 in the RNAseq analyses; and =3 in the proteomics analyses). The selected sets were tested for enrichment using Fisher's exact test. Multiple testing correction was performed using the qvalue R package (Storey et al., 2023). Terms with a FDR < 0.1 and an odds ratio > 2 were selected for visualization in figures 3D, and 4D, where node sizes was proportional to the significance of the enrichments. In these visualizations, two terms were connected depending on the amount of sharing between the groups of genes contributing to the enrichments in each of them, drawing a link whenever the intersection between the groups of genes was larger than 50% of the smallest of the two gene sets involved. Ontology term clusters, represented by colors, were then assigned using the Louvain's algorithm for modularity optimization (Blondel et al., 2008), as implemented in the R package igraph (Csardi and Nepusz, 2006). Visualization of the resulting networks was done using the open-source software Gephi (Bastian et al., 2009).

Targeted metabolomics. LC-MS analysis was carried out on a Schimazdu LC/MS-8030 coupled with a triple quadrupole mass analyser (QqQ) provided with an electrospray source in a negative ionization mode. Extracted metabolites were quantified in Multiple Reaction Monitoring (MRM) mode. A stock standard solution prepared in 17% (v/v) methanol in water and containing all metabolites: acetyl-CoA, methyl citrate, methylmalonyl-CoA, pyruvate, was used as external standard. Metabolites were identified by ion pairing liquid chromatography. Acetyl-CoA, methyl citrate and methylmalonyl-CoA were separated by reverse phase with a poroshell 120 Phenyl-Hexyl analytical column (2.1 x 50mm, 2.7 µm, Agilent) and a binary gradient (**Table S2**) consisting of a mobile phase A with water-methanol 97:3 (v/v), 10 mM

tributylamine and 3 mM acetic acid, and mobile phase B composed of pure methanol. Pyruvate was separated by normal phase using a Kinetex HILIC analytical column (2.1 x 150 mm, 2.6 µm, Phenomenex) and a binary gradient (**Table S3**) consisting of pure water as mobile phase A and pure methanol as mobile phase B.

The flow rate was maintained at 0.4 ml/min and the injection volume was 20 µl. Nitrogen was used as nebulizing and drying gas at a flow rate of 1.5 and 15 ml/min, respectively. The desolvation line (DL) temperature was set at 250°C and the ionization voltage was fixed at 4.5 kV. Argon was used as collision gas to perform collision-induced dissociation at a pressure of 230 kPa. The dwell time was set at 100 ms and the detection was performed in MRM mode (detector voltage of 1.8 Kv), monitoring three transitions for each compound. The transition with higher intensity was selected as quantitative purposes (**Table S4**), while the other two were used for confirmation of the identity.

Lipidomic analysis by UPLC-MS. The effect of virR on relative abundance of different cell wall lipids was characterized as had been done previously for MEVs (Prados-Rosales et al., 2014b). Briefly, cell wall lipids were extracted from triplicate 10 ml cultures of wild type, *virR*^{mut}, and *virR*^{mut} complemented (*virR*^{mut}-C) strains overnight into 3 ml 2:1 chloroform:methanol at room temperature, extracts were dried under nitrogen before being dissolved in 0.75 ml LC-MS grade 2:1:1 isopropanol:acetonitrile:water. Extracts were separated on a Waters ACQUITY BEH C18 column UPLC heated to 55ºC and eluted at a flow rate of 0.4 ml/minute with 60:40 acetonitrile:water as mobile phase A and 90:10 isopropanol:acetonitrile as mobile phase B, both containing 10 mM ammonium formate and 0.1% formic acid. Initial condition was 40%, B which increased to 43% at 2 minutes, 50% at 2.1 minutes, 54% at 12 minutes, 70% at 12.1 minutes, 90% at 18 minutes before returning to initial condition at 18.1 minutes to complete the run at 20 minutes. The coupled Waters Synapt G2 q-TOF MS was operated in positive ion resolution mode with the following conditions: capillary voltage 2kV, cone voltage 30V, desolvation gas temperature 550°C , gas flow 900L/hour, source temperature 120°C. Mass spectra were acquired in centroid mode from 100-3000 m/z with scan times of 0.5 second. Leucine enkephaline was used as reference. Relative abundances of Mass-retention time pairs were normalized to total ion current and lipid species were identified using Mycomass (Layre et al., 2011) and Mtb LipidDB databases (Sartain et al., 2011).

Lipidomic analysis by thin layer chromatography (TLC). Lipidomic analysis of both whole cells and EVs by TLC was performed as previously described (Boldrin et al.,

2021). *Mtb* strains were grown at 37°C in standing Middlebrook 7H9 and when they reached an OD595 of 0.2, cells were washed and transferred to MM. Cells were grown until they reached an OD595 of 0.5. Further, cells were harvested by centrifugation at 3,500 rpm for 5 min, and pellets were heat-inactivated at 100°C for 1 h and used for lipid extraction. Five milliliters 2:1 (vol/vol) chloroform-methanol was added to the cell pellet and incubated at room temperature (RT) for 12 h with constant stirring. The organic extract was separated by centrifugation (1,000 × g, 5 min, RT) and decantation. The obtained pellet was extracted with 5 ml 2:1 (vol/vol) chloroform-methanol for 1 h at RT with constant stirring and separated under the same conditions. The combined two organic extracts (total lipids) were dried under a stream of nitrogen gas at RT and saved for lipid analysis.

Polar lipids were separated by 2D-TLC by spotting 200 µg of total lipids on 60 F254 silica gel plates (Merck) using chloroform, methanol, water (50:30:6) as a mobile phase 1 (first dimension), and chloroform, acetic acid, methanol, and water (40:25:3:6) as mobile phase 2 (second dimension). Analysis of PDIMs and TAGs was performed in a 1D-TLC format. Two hundred µg of total lipids were spotted on the silica plates and separated using 9:1 petroleum ether-diethyl ether as mobile phase. Free mycolates were separated by 1D-TLC using chloroform/methanol/ammonium hydroxide (80:20:2) as mobile phase. Mycolic acids were extracted and separated from cells as previously described (Vilchèze and Jacobs, 2007). EV-associated lipids were separated and visualized following the same procedures as for WCLs. Development of TLC plates was performed by repeating the process of pulverizing the staining solution and heating the plate at 100°C 4 times. The staining solution contained 10.5 ml 15% ethanolic solution of 1-naphthol, 6.5 ml 97% sulfuric acid, 40.5 ml ethanol, and 4 ml water.

PG isolation. To obtain mycobacterial cell walls, whole cell pellets were resuspended in PBS and boiled for 15 min. Boiled cells were transferred to 2 ml Lysing matrix tubes with 0.1 mm silica beads (M.P. Biomedical, Santa Ana, CA, United States). And mechanically disrupted in a FastPrep-24TM (M.P. Biomedical) giving 12 cycles at predetermined speed of 6 during 30 sec. Samples were allowed to chill on ice for 3 min between cycles. Cell breakage was monitored by optical microscopy (using Methylene blue as stain), if 95% of the cells had not broken perform additional FastPrep-24TM cycles were performed. Lysed cells were centrifuged at 170 × g for 30 sec to separate them from beads and the supernatant were transferred to a clean 1.5 ml tube. The suspensions were further digested with 10 µg of DNase and RNase/ml for 1 h at 4°C to obtain a cell wall-enriched fraction after centrifugation at 27,000 × g for 10 min. Cell walls were resuspended in PBS containing 2% sodium dodecyl sulfate (SDS) and

the suspension was incubated for 1 h at 90 °C with constant stirring and recentrifuged at 27,000 × g for 30 min, and the supernatant was discarded. This process was repeated twice. The resulting pellet was washed trice in distilled water, 80% acetone and acetone and lyophilized. Pellets were resuspended in 0.9 ml Tris-HCL (50 mM, pH 7) buffer, plus 0.1 ml of protease K stock solution. The mixture was incubated at 60 °C for 90 min, to digest any remaining surface proteins attached to the CW and centrifuged again for 3 min at 20,000 × g and resuspend pellet in distilled water. The mixture was then heated at 90°C for 1 h before centrifugation at 27,000 × g for 30 min. The supernatant was discarded and washed twice with PBS and four times with deionized water to remove SDS. Pure PG was obtained from isolated cell walls. Briefly, pure cell walls were resuspended in 0.5% KOH in methanol and stirred at 37°C for 4 days to hydrolyze mycolic acids (MA). The mixture was centrifuged (27,000 × g 20 min) and the pellet was washed twice with methanol. MA were separated from cell walls using diethyl ether and recentrifuged at 27,000 × gfor 20 min. The supernatant contained MAMEs. The extraction process with diethyl ether was repeated twice and let dry. The resulting arabinogalactan (AG)-PG was digested with 0.2 N H2SO4 at 85°C for 30 min and neutralized with $BaCO_3$ to remove the arabinogalactan. Treated AG-PG was centrifuged at 27,000 × g for 20 min. Supernatant contained soluble AG. The resulting insoluble PG was washed four times by centrifugation in deionized water and stored at 4°C or room temperature.

Analysis of diaminopimelic acid. For DAP quantification (Tsuruoka et al., 1985), samples were hydrolyzed overnight in 6N HCl at 100°C in 1 ml capacity-crystal ampoules (Wheaton). Samples were dried and resuspended in water and mixed in a 1:1:1 ratio with pure acetic acid and ninhydrin reagent (250 mg ninhydrin, 4 ml phosphoric acid 0.6 M, and 6 ml pure acetic acid). Samples were measured at OD 434nm, and the amounts of DAP were calculated based on a standard curve with pure DAP. The data displays the average ± standard deviations n=3.

Glycosyl composition of isolated cell walls. 500 µg of purified cell walls were mixed with 10 µg of inositol and hydrolyzed with 0.1 M trifluoroacetic acid (TFA) for 2 h at 121°C. The monosaccharides released were then converted into alditol acetates by reduction with $NaBH_4$ and acetylation with acetic anhydride in pyridine. The products were analyzed by gas chromatography-mass spectrometry in a 7890A/5975C system from Agilent, using a DB-5ht (30 m x 0.25 mm x 0.1 µm) fused silica capillary column. The compounds were identified by comparing the retention times of the peaks with those recorded for standards analyzed under identical conditions. Quantification was

carried out considering the area of the peaks and the response factors of each compound with respect to inositol.

Atomic force microscopy and data analysis. The dry pellets of purified peptidoglycan from the three strains were dissolved in pure water and further broken by tip sonication at 2 mA for 30 sec, three cycles. Then 10 µl of the PG suspension was added to standard AFM substrate made of mica coated with 0.01 % Poly-L-lysine by incubating the sample during 90 min to achieve good coverage. The sample was further rinsed with water and dried with Nitrogen flow. The AFM in ambient conditions (i.e. air) was performed using Tapping mode in a Bruker FastScan Bio machine (Santa Barbara, CA, United States) with Nunano SCOUT 350 - Silicon AFM probes (spring constant: 42 N/m, Resonance frequency: 350 kHz). The images were taken using a free amplitude of 10 nm with set point of 70-80 % of free amplitude (e.g. 7 nm). For AFM high resolution imaging in liquid the images were acquired in Peak force Tapping mode in imaging buffer made of 10 mM Tris and 150 mM KCl, pH: 8, with the FastScan Bio machine using Bruker Fastscan-D AFM probes (spring constant: 0.1 N/m, Resonance frequency: 70 kHz) at the force range of 1-3 nN peak force set point. The imaging parameters used are as follows; Scan rate: 1 Hz; Scan angle: 0 °; Peak force amplitude: 80-100 nm and with high pixel resolution (512-880).

The thickness measurements were performed with standard Gwyddion 1D height distribution tool (selecting an area containing background and a single leaflet of peptidoglycan). The number of cells analysed varied from n = 23 (for Mtb WT), n = 36 (for *virR*^{mut}) and n = 25 (for *virR*^{mut}-C). The comparisons extracted from this data is statistically relevant with t test with Welch's correction performed. The analysis of the high-resolution images obtained in liquid was performed using the semi-automated custom-made routine from (Pasquina-Lemonche, et al. "Pore AFM", 2024) where the pore area, later converted in diameter, and the pore number were measured from the 2D slice of each image containing the maximum number of pores (see **Fig. S8**). The number of images similar to images shown in **Fig. 5** were n = 8 for all strains, analyzing both pore size and pore number, the statistical comparisons were also performed using a t test with Welch's correction.

Blue native PAGE. Oligomerization of VirR and Lcp1 was analyzed by Blue native PAGE (Invitrogen, Waltham, MA, United States). Recombinant VirR and Lcp1 proteins were prepared in 1xLB Native PAGE including DDM at 0.5% final concentration. After incubation at 4ºC for 30 min, samples were centrifuged at 20,000 × g for 30 min at 4°C. The supernatant was recovered and mixed with G-250 additive following manufacturer

instructions (Invitrogen) and loaded onto a Novex® Bist-Tris 4-16% gradient gel and run following manufacturer instructions. Gel was first fixed and then stained with Coomassie.

Liposome flotation assay. Individual or combined VirR and Lcp1 were prepared at 2 µM in buffer A in a final volume of 50 µl and incubated for 30 min at 37°C. This volume was mixed with 100 µl of 60% optiprep (Sigma-Aldrich) to a final concentration of 40% and overlaid with 100 µl of subsequent optiprep solutions at 35%, 30%, 20% and 10% (optiprep solutions were prepared in Buffer A). The samples were centrifugated at 70000 rpm for 2 h at 4°C in an Optima TLX Ultracentrifuge (Beckman Coulter, Indianapolis, IN United States). Eleven fractions of 50 µl were recovered and examined by dot blot (performed as previously described). Polyclonal antibodies raised against VirR and Lcp1 were used as primary antibodies. Quantification of dotblots was performed in ImageJ as previously described (Schirmer et al., 2022). Briefly, integrated densities were calculated after background subtraction, and referred to wild type values to obtain the relative integrated intensities.

Lysozyme and PG and AG susceptibility assays. *Mtb* WT and *virR*^{mut} strains were grown in 7H9 media supplemented with ADC and Tween 80 to an OD 540 of 0.2 and then diluted to an OD540 of 0.1 with 7H9 containing 0 or 50 µgml^{-1} lysozyme (Sigma). The cultures were incubated with agitation at 37°C and OD540 was monitored daily.

Fluorescence microscopy. The *Mtb* strain bearing the plasmid VirR-pMV261-Venus was grown in MM to an OD595nm of 0.4. At this stage, cells were harvested, washed three times in 1 × PBS (pH 7.4), resuspended in 1/3 – 1/6 volume of 4% paraformaldehyde (PFA) and incubated for 2 h at 37 °C. Finally, the cells were washed twice in 1 × PBS and resuspended in 100–200 µl of PBS. Microscope slides were covered with 5 µl poly-L-lysine (Sigma) and excess poly-L-lysine was removed away with distillated water. A 20 – 40 µl aliquot was applied to pre-treated slides, allowed to air dry and covered with antifade solution (Prolong Gold, Invitrogen) and visualized under the fluorescence microscope using a 100x oil immersion objective on an Orca 12-ERG digital CCD camera (Hamamatsu Photonics) mounted on a Nikon E600 microscope.

FACS analysis for split-GFP experiments. *M. smegmatis* mc²155 transformed with the pGMCS derivatives were inoculated in complete 7H9 medium. After overnight incubation at 37°C, bacteria were collected and analyzed by fluorescence activated cell

sorting using a BD FACS LSRFortessa X20 flow cytometer. Flow cytometry data analysis was performed using FlowJo software (Version 10; Becton, Dickinson and Company, Ashland, OR, United States). The gating strategy is displayed in supplementary figure 10 (**Fig. S10**).

Statistical analysis. The statistical significance of the difference between experimental groups was determined by the two-tailed Student's test using PRISM 5.0. P values ≤ than 0.05 were considered significant. Statistical analysis of RNAseq is detailed in the corresponding section of Materials and Methods.

Data Availability. The Datasets produced in this study are available in the following database: RNA-seq data: Gene expression Omnibus, GSE143996 (https://www.ncbi.nlm.nih.gov/geo/query/acc.cgi?acc=GSE143996).

Funding Information. R.P.-R. acknowledges support by MINECO/FEDER EU contracts SAF2016–77433-R, PID2019-110240RB-I00, PID2022-136611OB-I00; and NIH-R01AI162821. CICbioGUNE thanks MINECO for the Severo Ochoa Excellence Accreditation (SEV-2016–0644). L.P-L and J.K.H acknowledges support by the Wellcome Trust (212197/Z/19/Z) which funded part of this research. For the purpose of open access, the authors have applied and will apply a CC BY public copyright license to any Author Accepted Manuscript version arising from this submission. J.S. acknowledges support from the Spanish Ministry of Science and Innovation (MICINN) through grant PID2019-106859GA-I00 and Ramón y Cajal research grant RYC-2017-23560, as well as to the Government of Aragón, Spain, through grant B49-23R (NeuroBioSys). FC lab research is supported by the Swedish Research Council (VR2018-02823 and VR2018-05882), the Laboratory for Molecular Infection Medicine Sweden (MIMS), Umeå University, the Knut and Alice Wallenberg Foundation (KAW) grant KAW2012.0184 and the Kempe Foundation.

Acknowledgments. We are very grateful to Carl Nathan for sharing mutant *Mtb* strains. We thank G. Marcela Rodriguez for sharing the a-IdeR antibody. We thank Heran Darwin for sharing a-cei polyclonal antibody. We thank Emmanuelle Näser (Génotoul TRI-IPBS platform, Toulouse) for helping with flow cytometry. We thank Dr. Luke Alderwick (University of Birmingham) for the donation of the plasmid to recombinantly express Lcp1 protein. We thank M. Gutiérrez for assistance with figures. The authors have no conflict of interest to declare.

References

Amaral L, Kristiansen JE, Abebe LS, Millett W. 1996. Inhibition of the respiration of multi-drug resistant clinical isolates of Mycobacterium tuberculosis by thioridazine: Potential use for initial therapy of freshly diagnosed tuberculosis. *J Antimicrob Chemother* **38**. doi:10.1093/jac/38.6.1049

Ariyachaokun K, Grabowska AD, Gutierrez C, Neyrolles O. 2020. Multi-stress induction of the Mycobacterium tuberculosis MbcTA bactericidal toxin-antitoxin system. *Toxins (Basel)* **12**. doi:10.3390/toxins12050329

Athman JJ, Sande OJ, Groft SG, Reba SM, Nagy N, Wearsch PA, Richardson ET, Rojas R, Boom WH, Shukla S, Harding C V. 2017. Mycobacterium tuberculosis Membrane Vesicles Inhibit T Cell Activation. *J Immunol* **198**:2028–2037. doi:10.4049/jimmunol.1601199

Athman JJ, Wang Y, McDonald DJ, Boom WH, Harding C V, Wearsch PA. 2015. Bacterial Membrane Vesicles Mediate the Release of Mycobacterium tuberculosis Lipoglycans and Lipoproteins from Infected Macrophages. *J Immunol* **195**:1044–1053. doi:10.4049/jimmunol.1402894

Ballister ER, Samanovic MI, Darwin KH. 2019. Mycobacterium tuberculosis rv2700 contributes to cell envelope integrity and virulence. *J Bacteriol* **201**. doi:10.1128/JB.00228-19

Bastian M, Heymann S, Jacomy M. 2009. Gephi: An Open Source Software for Exploring and Manipulating Networks. *Proc Int AAAI Conf Web Soc Media* **3**. doi:10.1609/icwsm.v3i1.13937

Baumgart M, Schubert K, Bramkamp M, Frunzke J. 2016. Impact of LytRCpsA-Psr proteins on cell wall biosynthesis in Corynebacterium glutamicum. *J Bacteriol* **198**. doi:10.1128/JB.00406-16

Beaulieu AM, Rath P, Imhof M, Siddall ME, Roberts J, Schnappinger D, Nathan CF. 2010. Genome-wide screen for Mycobacterium tuberculosis genes that regulate host immunity. *PLoS One* **5**:e15120. doi:10.1371/journal.pone.0015120

Blondel VD, Guillaume J-L, Lambiotte R, Lefebre E. 2008. Fast unfolding of community hierarchies in large networks. *J Stat Mech Theory Exp* **10**.

Boldrin F, Anso I, Alebouyeh S, Sevilla IA, Geijo M, Garrido JM, Marina A, Mazzabò LC, Segafreddo G, Guerin ME, Manganelli R, Prados-Rosales R. 2021. The phosphatidyl-myo-inositol dimannoside acyltransferase pata is essential for mycobacterium tuberculosis growth in vitro and in vivo. *J Bacteriol* **203**. doi:10.1128/JB.00439-20

Boudehen YM, Faucher M, Maréchal X, Miras R, Rech J, Rombouts Y, Sénèque O, Wallat M, Demange P, Bouet JY, Saurel O, Catty P, Gutierrez C, Neyrolles O.

2022. Mycobacterial resistance to zinc poisoning requires assembly of P-ATPase-containing membrane metal efflux platforms. *Nat Commun* **13**. doi:10.1038/s41467-022-32085-7

Brzostek A, Pawelczyk J, Rumijowska-Galewicz A, Dziadek B, Dziadek J. 2009. Mycobacterium tuberculosis is able to accumulate and utilize cholesterol. *J Bacteriol* **191**. doi:10.1128/JB.00488-09

Cabantous S, Nguyen HB, Pedelacq JD, Koraïchi F, Chaudhary A, Ganguly K, Lockard MA, Favre G, Terwilliger TC, Waldo GS. 2013. A new protein-protein interaction sensor based on tripartite split-GFP association. *Sci Rep* **3**. doi:10.1038/srep02854

Csardi G, Nepusz T. 2006. The igraph software package for complex network research. *InterJournal Complex Syst* **Complex Sy**.

De Keijzer J, Mulder A, De Haas PEW, De Ru AH, Heerkens EM, Amaral L, Van Soolingen D, Van Veelen PA. 2016. Thioridazine alters the cell-envelope permeability of mycobacterium tuberculosis. *J Proteome Res* **15**. doi:10.1021/acs.jproteome.5b01037

De Knegt GJ, Ten Kate MT, Van Soolingen D, Aarnoutse R, Boeree MJ, Bakker-Woudenberg IAJM, De Steenwinkel JEM. 2014. Enhancement of in vitro activity of tuberculosis drugs by addition of thioridazine is not reflected by improved in vivo therapeutic efficacy. *Tuberculosis* **94**. doi:10.1016/j.tube.2014.09.002

Dutta NK, Mehra S, Kaushal D. 2010. A Mycobacterium tuberculosis sigma factor network responds to cell-envelope damage by the promising anti-mycobacterial thioridazine. *PLoS One* **5**. doi:10.1371/journal.pone.0010069

Ghazaei C. 2018. Mycobacterium tuberculosis and lipids: Insights into molecular mechanisms from persistence to virulence. *J Res Med Sci*. doi:10.4103/jrms.JRMS_904_17

Grzegorzewicz AE, de Sousa-d'Auria C, McNeil MR, Huc-Claustre E, Jones V, Petit C, Angala SK, Zemanova J, Wang Q, Belardinelli JM, Gao Q, Ishizaki Y, Mikusova K, Brennan PJ, Ronning DR, Chami M, Houssin C, Jackson M. 2016. Assembling of the Mycobacterium tuberculosis Cell Wall Core. *J Biol Chem* **291**:18867–18879. doi:10.1074/jbc.M116.739227

Gupta S, Bhagavathula, M Sharma V, Sharma N, Sharma N, Biswas A, Palacios A, Salgueiro V, Lavín J, Dogra N, Salgame P, Prados-Rosales, R Rodríguez G. 2023. Dynamin-like proteins mediate extracellular vesicle secretion in Mycobacterium tuberculosis. *EMBO Rep* **24**:e55593.

Harrison J, Lloyd G, Joe M, Lowary TL, Reynolds E, Walters-Morgan H, Bhatt A, Lovering A, Besra GS, Alderwick LJ. 2016. Lcp1 is a phosphotransferase

responsible for ligating arabinogalactan to peptidoglycan in mycobacterium tuberculosis. *MBio* **7**. doi:10.1128/mBio.00972-16

Honaker RW, Leistikow RL, Bartek IL, Voskui MI. 2009. Unique roles of DosT and DosS in DosR regulon induction and Mycobacterium tuberculosis dormancy. *Infect Immun* **77**. doi:10.1128/IAI.01449-08

Huber W, Heydebreck A Von, Ultmann HS¨, Poustka A, Vingron M. 2002. Variance stabilization applied to microarray data calibration and to the quantification of differential expression. *BIOINFORMATICS*.

Hubscher J, Luthy L, Berger-Bachi B, Stutzmann Meier P. 2008. Phylogenetic distribution and membrane topology of the LytR-CpsA-Psr protein family. *BMC Genomics* **9**:617. doi:10.1186/1471-2164-9-617

Justen AM, Hodges HL, Kim LM, Sadecki PW, Porfirio S, Ultee E, Black I, Chung GS, Briegel A, Azadi P, Kiessling LL. 2020. Polysaccharide length affects mycobacterial cell shape and antibiotic susceptibility. *Sci Adv* **6**. doi:10.1126/sciadv.aba4015

Kalscheuer R, Palacios A, Anso I, Cifuente J, Anguita J, Jacobs Jr. WR, Guerin ME, Prados-Rosales R. 2019. The Mycobacterium tuberculosis capsule: a cell structure with key implications in pathogenesis. *Biochem J* **476**:1995–2016. doi:10.1042/BCJ20190324

Kawai Y, Marles-Wright J, Cleverley RM, Emmins R, Ishikawa S, Kuwano M, Heinz N, Bui NK, Hoyland CN, Ogasawara N, Lewis RJ, Vollmer W, Daniel RA, Errington J. 2011. A widespread family of bacterial cell wall assembly proteins. *EMBO J* **30**:4931–4941. doi:10.1038/emboj.2011.358

Layre E, Sweet L, Hong S, Madigan CA, Desjardins D, Young DC, Cheng TY, Annand JW, Kim K, Shamputa IC, McConnell MJ, Debono CA, Behar SM, Minnaard AJ, Murray M, Barry CE, Matsunaga I, Moody DB. 2011. A comparative lipidomics platform for chemotaxonomic analysis of mycobacterium tuberculosis. *Chem Biol* **18**. doi:10.1016/j.chembiol.2011.10.013

Lee JE, Moon PG, Lee IK, Baek MC. 2015. Proteomic Analysis of Extracellular Vesicles Released by Adipocytes of Otsuka Long-Evans Tokushima Fatty (OLETF) Rats. *Protein J* **34**:220–235. doi:10.1007/s10930-015-9616-z

Lee W, VanderVen BC, Fahey RJ, Russell DG. 2013. Intracellular Mycobacterium tuberculosis exploits host-derived fatty acids to limit metabolic stress. *J Biol Chem* **288**:6788–6800. doi:10.1074/jbc.M112.445056

Li C, Wen A, Shen B, Lu J, Huang Y, Chang Y. 2011. FastCloning: A highly simplified, purification-free, sequence- and ligation-independent PCR cloning method. *BMC Biotechnol* **11**. doi:10.1186/1472-6750-11-92

Liao Y, Smyth GK, Shi W. 2019. The R package Rsubread is easier, faster, cheaper and better for alignment and quantification of RNA sequencing reads. *Nucleic Acids Res* **47**. doi:10.1093/nar/gkz114

Love MI, Huber W, Anders S. 2014. Moderated estimation of fold change and dispersion for RNA-seq data with DESeq2. *Genome Biol* **15**. doi:10.1186/s13059-014-0550-8

Majlessi L, Prados-Rosales R, Casadevall A, Brosch R. 2015. Release of mycobacterial antigens. *Immunol Rev* **264**:25–45. doi:10.1111/imr.12251

Marsollier L, Brodin P, Jackson M, Kordulakova J, Tafelmeyer P, Carbonnelle E, Aubry J, Milon G, Legras P, Andre JP, Leroy C, Cottin J, Guillou MLJ, Reysset G, Cole ST, Korduláková J, Tafelmeyer P, Carbonnelle E, Aubry J, Milon G, Legras P, Saint André JP, Leroy C, Cottin J, Guillou MLJ, Reysset G, Cole ST. 2007. Impact of Mycobacterium ulcerans biofilm on transmissibility to ecological niches and Buruli ulcer pathogenesis. *PLoS Pathog* **3**:e62. doi:10.1371/journal.ppat.0030062

McMillan HM, Kuehn MJ. 2021. The extracellular vesicle generation paradox: a bacterial point of view. *EMBO J* **40**. doi:10.15252/embj.2021108174

Mohammadzadeh R, Ghazvini K, Farsiani H, Soleimanpour S. 2021. Mycobacterium tuberculosis extracellular vesicles: exploitation for vaccine technology and diagnostic methods. *Crit Rev Microbiol*. doi:10.1080/1040841X.2020.1830749

Nagakubo T, Tahara YO, Miyata M, Nomura N, Toyofuku M. 2021. Mycolic acid-containing bacteria trigger distinct types of membrane vesicles through different routes. *iScience* **24**. doi:10.1016/j.isci.2020.102015

Nagamani S, Sastry GN. 2021. Mycobacterium tuberculosis cell wall permeability model generation using chemoinformatics and machine learning approaches. *ACS Omega* **6**. doi:10.1021/acsomega.1c01865

Nečas D, Klapetek P. 2012. Gwyddion: An open-source software for SPM data analysis. *Cent Eur J Phys*. doi:10.2478/s11534-011-0096-2

Oba S, Sato MA, Takemasa I, Monden M, Matsubara KI, Ishii S. 2003. A Bayesian missing value estimation method for gene expression profile data. *Bioinformatics* **19**:2088–2096. doi:10.1093/bioinformatics/btg287

Pandey R, Rodriguez GM. 2014. IdeR is required for iron homeostasis and virulence in Mycobacterium tuberculosis. *Mol Microbiol* **91**. doi:10.1111/mmi.12441

Pasquina-Lemonche L, Burns J, Turner RD, Kumar S, Tank R, Mullin N, Wilson JS, Chakrabarti B, Bullough PA, Foster SJ, Hobbs JK. 2020. The architecture of the Gram-positive bacterial cell wall. *Nature* **582**. doi:10.1038/s41586-020-2236-6

Pawełczyk J, Brzostek A, Minias A, Płociński P, Rumijowska-Galewicz A, Strapagiel D, Zakrzewska-Czerwińska J, Dziadek J. 2021. Cholesterol-dependent transcriptome

remodeling reveals new insight into the contribution of cholesterol to Mycobacterium tuberculosis pathogenesis. *Sci Rep* **11**. doi:10.1038/s41598-021-91812-0

Prados-Rosales R, Baena A, Martinez LR, Luque-Garcia J, Kalscheuer R, Veeraraghavan U, Camara C, Nosanchuk JD, Besra GS, Chen B, Jimenez J, Glatman-Freedman A, Jacobs Jr. WR, Porcelli SA, Casadevall A. 2011. Mycobacteria release active membrane vesicles that modulate immune responses in a TLR2-dependent manner in mice. *J Clin Invest* **121**:1471–1483. doi:10.1172/JCI44261

Prados-Rosales Rafael, Baena A, Martinez LR, Luque-Garcia J, Kalscheuer R, Veeraraghavan U, Camara C, Nosanchuk JD, Besra GS, Chen B, Jimenez J, Glatman-Freedman A, Jacobs Jr. WR, Porcelli SA, Casadevall A, Jacobs WR, Porcelli SA, Casadevall A. 2011. Mycobacteria release active membrane vesicles that modulate immune responses in a TLR2-dependent manner in mice. *J Clin Invest* **121**:1471–1483. doi:10.1172/JCI44261

Prados-Rosales R, Carreno L, Cheng T, Blanc C, Weinrick B, Malek A, Lowary TL, Baena A, Joe M, Bai Y, Kalscheuer R, Batista-Gonzalez A, Saavedra NA, Sampedro L, Tomas J, Anguita J, Hung SC, Tripathi A, Xu J, Glatman-Freedman A, Jacobs Jr. WR, Chan J, Porcelli SA, Achkar JM, Casadevall A. 2017. Enhanced control of Mycobacterium tuberculosis extrapulmonary dissemination in mice by an arabinomannan-protein conjugate vaccine. *PLoS Pathog* **13**:e1006250. doi:10.1371/journal.ppat.1006250

Prados-Rosales R, Carreño LJ, Batista-Gonzalez A, Baena A, Venkataswamy MM, Xu J, Yu X, Wallstrom G, Mitchell Magee D, LaBaer J, Achkar JM, Jacobs WR, Chan J, Porcelli SA, Casadevall A. 2014a. Mycobacterial membrane vesicles administered systemically in mice induce a protective immune response to surface compartments of mycobacterium tuberculosis. *MBio* **5**:e01921-14. doi:10.1128/mBio.01921-14

Prados-Rosales R, Weinrick BC, Pique DG, Jacobs Jr. WR, Casadevall A, Rodriguez GM, Piqué DG, Jacobs WR, Casadevall A, Rodriguez GM. 2014b. Role for Mycobacterium tuberculosis membrane vesicles in iron acquisition. *J Bacteriol* **196**:1250–1256. doi:10.1128/JB.01090-13

Prasad TSK, Verma R, Kumar S, Nirujogi RS, Sathe GJ, Madugundu AK, Sharma J, Puttamallesh VN, Ganjiwale A, Myneedu VP, Chatterjee A, Pandey A, Harsha HC, Narayana J. 2013. Proteomic analysis of purified protein derivative of mycobacterium tuberculosis. *Clin Proteomics* **10**. doi:10.1186/1559-0275-10-8

Rath P, Huang C, Wang T, Wang T, Li H, Prados-Rosales R, Elemento O, Casadevall

A, Nathan CF. 2013. Genetic regulation of vesiculogenesis and immunomodulation in Mycobacterium tuberculosis. *Proc Natl Acad Sci U S A* **110**:E4790-7. doi:10.1073/pnas.1320118110

Ritchie ME, Phipson B, Wu D, Hu Y, Law CW, Shi W, Smyth GK. 2015. Limma powers differential expression analyses for RNA-sequencing and microarray studies. *Nucleic Acids Res* **43**:e47. doi:10.1093/nar/gkv007

Rock JM, Hopkins FF, Chavez A, Diallo M, Chase MR, Gerrick ER, Pritchard JR, Church GM, Rubin EJ, Sassetti CM, Schnappinger D, Fortune SM. 2017. Programmable transcriptional repression in mycobacteria using an orthogonal CRISPR interference platform. *Nat Microbiol* **2**:16274. doi:10.1038/nmicrobiol.2016.274

Sani M, Houben ENG, Geurtsen J, Pierson J, De Punder K, Van Zon M, Wever B, Piersma SR, Jiménez CR, Daffé M, Appelmelk BJ, Bitter W, Van Wel N Der, Peters PJ. 2010. Direct visualization by Cryo-EM of the mycobacterial capsular layer: A labile structure containing ESX-1-secreted proteins. *PLoS Pathog* **6**. doi:10.1371/journal.ppat.1000794

Sartain MJ, Dick DL, Rithner CD, Crick DC, Belisle JT. 2011. Lipidomic analyses of Mycobacterium tuberculosis based on accurate mass measurements and the novel “Mtb LipidDB.” *J Lipid Res* **52**. doi:10.1194/jlr.M010363

Schirmer S, Rauh L, Alebouyeh S, Delgado-Velandia M, Salgueiro VC, Lerma L, Serrano-Mestre JL, Azkargorta M, Elortza F, Lavín JL, García MJ, Tórtola-Fernández MT, Gola S, Prados-Rosales R. 2022. Immunogenicity of Mycobacterial Extracellular Vesicles Isolated From Host-Related Conditions Informs About Tuberculosis Disease Status. *Front Microbiol* **13**:907296. doi:10.3389/fmicb.2022.907296

Schnappinger D, Ehrt S, Voskuil MI, Liu Y, Mangan JA, Monahan IM, Dolganov G, Efron B, Butcher PD, Nathan C, Schoolnik GK. 2003. Transcriptional adaptation of Mycobacterium tuberculosis within macrophages: Insights into the phagosomal environment. *J Exp Med* **198**. doi:10.1084/jem.20030846

Storey JD, Bass AJ, Dabney A, Robinson D. 2023. qvalue: Q-value estimation for false discovery rate control.

Trapnell C, Pachter L, Salzberg SL. 2009. TopHat: Discovering splice junctions with RNA-Seq. *Bioinformatics* **25**. doi:10.1093/bioinformatics/btp120

Tsuruoka T, Tamura A, Miyata A, Takei T, Inouye S, Matsuhashi M. 1985. Second Lytic Target of Beta-Lactam Compounds That Have A Terminal d-Amino Acid Residue. *Eur J Biochem* **151**. doi:10.1111/j.1432-1033.1985.tb09090.x

Vilchèze C, Jacobs WR. 2007. Isolation and analysis of Mycobacterium tuberculosis

mycolic acids. *Curr Protoc Microbiol* **Chapter 10**. doi:10.1002/9780471729259.mc10a03s05

Wang M, Guo X, Yang X, Zhang B, Ren J, Liu A, Ran Y, Yan B, Chen F, Guddat LW, Hu J, Li J, Rao Z. 2019. Mycobacterial dynamin-like protein IniA mediates membrane fission. *Nat Commun* **10**. doi:10.1038/s41467-019-11860-z

White DW, Elliott SR, Odean E, Bemis LT, Tischler AD. 2018. Mycobacterium tuberculosis Pst/SenX3-RegX3 Regulates Membrane Vesicle Production Independently of ESX-5 Activity. *MBio* **9**. doi:10.1128/mBio.00778-18

Wiśniewski JR, Zougman A, Nagaraj N, Mann M. 2009. Universal sample preparation method for proteome analysis. *Nat Methods* **6**. doi:10.1038/nmeth.1322

Zhang X, Smits AH, Tilburg GBA Van, Ovaa H, Huber W, Vermeulen M. 2018. Proteome-wide identification of ubiquitin interactions using UbIA-MS. *Nat Protoc* **13**:530–550. doi:10.1038/nprot.2017.147

Ziegenbalg A, Prados-Rosales R, Jenny-Avital ER, Kim RS, Casadevall A, Achkar JM. 2013. Immunogenicity of mycobacterial vesicles in humans: identification of a new tuberculosis antibody biomarker. *Tuberc* **93**:448–455. doi:10.1016/j.tube.2013.03.001

Zuber B, Haenni M, Ribeiro T, Minnig K, Lopes F, Moreillon P, Dubochet J. 2006. Granular layer in the periplasmic space of gram-positive bacteria and fine structures of Enterococcus gallinarum and Streptococcus gordonii septa revealed by cryo-electron microscopy of vitreous sections. *J Bacteriol* **188**. doi:10.1128/JB.00391-06

Figure Legends

Figure 1. Ultrastructural changes in the cell envelope of *virR*-deficient mutant associated with increased vesiculation. (**A**) Cryo-electron micrographs of indicated *Mtb* strains grown in high iron MM. Closed line rectangles were used to calculate grey value profiles of cell envelopes using ImageJ. The dashed line insets within the main micrograph were magnified to show a detailed view of the cell surface. Scale bars are 100 nm in main micrographs and 50 nm in the insets. (**B**) Density profiles based on grey values of the cross sections marked by solid line rectangles in A. (**C**) Mean values and standard errors of distances in nm between main cell envelope layers measured in A and C. *P < 0.05 after applying a Tukey´s multiple comparison test. The number of cells analyzed varied from n = 20 (WT), n = 15 ($virR^{mut}$) and n = 23 ($virR^{mut}$-C). CM, cytoplasmic membrane; OM, outer membrane; L1, layer 1; L2, layer 2.

Figure 2. Enhanced permeability and vesiculation are linked in the absence of LytR_C solo domain proteins in *Mtb*. (A) Uptake of ethidium bromide (EthBr) in the indicated strains, as measured by fluorescence at 590 nm for 65 min. Data are mean and standard deviation of three biological replicates. **(B)** Sensitivity of the indicated strains to different concentrations of vancomycin as measured by monitoring optical density at 580 nm (OD580) after 7 days. Data are mean and standard deviations of three biological replicated. Errors bars not shown are smaller than symbols. **(C)** Time course of the incorporation of FDAAs on the indicated strains in both 7H9 and MM as measured by fluorescence. Representative images of both WT and *virR*^{mut} strains in either 7H9 or MM at 8h after the addition of the FDAA. Data are mean and standard deviations of three biological replicates. The arrow indicates the time at which images were taken. Errors bar not shown are smaller than symbols. **(D)** immunoblot analysis of cell lysates of two independent conditional mutants (c1 and c2) for *virR* and *cei* for the presence of VirR and Cei proteins in cultures incubated with and without anhydrotetracycline (ATc). **(E)** Nanoparticle tracking analysis (NTA) of EV preparations derived from *virR* and *cei* conditional mutants (c2 (*virR*) and c1 (*cei*)) obtained from cultures with and without ATc showing number of particles per cm^3 determined by Zeta View NTA in three independent EV preparations. Data are presented as mean ± SEM.

Figure 3. Transcriptional profiling of *virR*^{mut} showcases systemic alterations in cell wall architecture and metabolism. (A) Experiment design for RNA-seq analyses. RNA was extracted from whole cell extracts from 4 replicate cultures of each strain (WT and *virR*^{mut}), and sequenced. Of these 8 samples, 7 passed quality control, (3 WT and 4 *virR*^{mut}) and were subsequently analyzed. **(B)** PCA plot of the transcriptomics data. The loadings from the two first principal components are plotted. PC1 (X axis) significantly separates samples across strains (One tailed Mann Whitney test: PC1 in WT vs *virR*^{mut}: p=2.86 e-02). **(C)** Number of differentially expressed genes between *virR*^{mut} and WT. *virR*^{mut} significantly affects expression of a total of 750+913=1663 genes, (Storey-Tibshirani FDR=5%), which represents 41.5% of all genes tested. **(D)** Gene Ontology (GO) enrichments of downregulated genes in *virR*^{mut} (left) and upregulated ones (right). GO terms selected for testing included biological process and cell compartment labels containing $N \geq 10$ genes, between levels 4-6 of the ontology tree. In this representation, each node in the networks represents a significantly enriched term (terms selected for visualization with FDR=10% and enrichment odds-ratio>2), nodes' size is proportional to the enrichment significance, and links between terms are added wherever the sets of genes contributing to the enrichments in a

connected pair show an intersection larger than 50% of the smallest of the gene sets involved in the pair (see Methods for further details, and supplementary table S2 for an extended list of all the enrichments found).

Figure 4. *virR* regulates the protein content of EVs in *Mtb*. (A). Experiment design for proteomics analyses. label-free mass spectrometry data was retrieved for three replicates of H37RV and *virR*^{mut}. For each strain, in turn, data corresponding to proteins extracted from either whole-cell extracts (WC) and EVs was produced, totaling 12 samples (2 strains times 2 cell compartments times 3 replicates). **(B)** PCA plot of the proteomics data. The loadings from the two first principal components are plotted. PC1 (X axis) significantly separates samples across cell-compartments (One-tailed Mann Withney test: PC1 in EVs vs WC: p= 1.08 e-03), while PC2 separates samples from EVs in *virR*^{mut} from the rest of samples (one-tailed Mann Withney test: PC2 in *virR*^{mut} in EV vs all other samples: p=4.55 e-03), indicating a differential peptidic cargo in the vesicles of *virR*^{mut}. **(C)** Bar plots of differentially expressed proteins found between strains in in whole cell extracts (left, 19 differentially expressed proteins at 5% FDR), and extracellular vesicles (right, 353 differentially expressed proteins at 5% FDR). **(D)** Gene Ontology enrichments of the downregulated proteins in the VirR mutant strain (left) and the upregulated ones (Right), at the EV location. GO terms selected for testing included biological process and cell compartment labels containing $N \geq 3$ genes, between levels 4-6 of the ontology tree. As in figure 3D, terms selected for visualization with FDR=10% and enrichment odds-ratio>2, nodes' size is proportional to the enrichment significance, and links between terms are added wherever the sets of proteins contributing to the enrichments in a connected pair shows an intersection larger than 50% of the smallest of the gene sets involved in the pair (see Methods for further details, and supplementary table S2 for an extended list of all the enrichments found). **(E)** Expression patterns of bacterioferritin proteins in the extracellular vesicles of WT and *virR*^{mut}. **(F)** Expression patterns of proteins contributing to enrichments of terms related to mycolic acids biosynthesis. **(G)** Bottom left: Concentrations of key metabolites in the propionyl-coA detoxification routes. Right: Metabolic pathway of the propionyl-coA detoxification route through the methyl-malonyl route, along with the differential expression statistics between the WT and *virR*^{mut} strains observed at transcriptomic and proteomic levels for the main enzymes involved. The framed plot represents the quantification of selected metabolites by mass spectrometry.

Figure 5. Cell permeability is a major driver of vesicle production in *Mtb*. (A) Time course of the uptake of ethidium bromide (EthBr) by *Mtb* grown in the indicated

conditions, as measured by fluorescence at 590 nm for 65 min. Data are mean and standard deviation of three biological replicates. **(B)** Dot-blot analysis of released EVs in supernatants from *Mtb* cultures submitted to the indicated conditions. The loading volume was normalized according to CFUs. The graph below represents the quantification of the dotblot using ImageJ. The integrated cell density was normalized to WT values. Data are mean and standard errors from the three biological replicates; **** denotes P<0.0001, *** denotes P=0.0028 after applying a Tukey´s multiple comparison test. **(C)** Enrichment odds ratios for Fisher exact tests comparing sets of genes up, and down regulated, respectively, in 1)cholesterol-supplemented medium vs. glucose-supplemented medium ((Pawełczyk et al., 2021), GEO accession GSE175812); and 2) *virR*^{mut} vs WT. **(D)** Euler diagram showing that 39 out of 48 genes in the DosR regulon are simultaneously repressed in *virR*^{mut} vs WT, and upregulated in cholesterol vs. glucose enriched medium cultures, suggesting a common activation of the regulon in conditions of low permeability (see also **Fig S5**). **(E)** Expression patterns in response to TRZ (1h) and in *virR*^{mut} for key genes involved in metal signaling, metabolism and homeostasis.

Figure 6. Lipidomic analysis of cell envelope and EVs from *virR*^{mut}. (A) Comparative total lipid analysis of the indicated strains by nano-LC-MS. Lipid species with an abundance higher than 0.5% are shown. Data indicates mean and standard error from three biological replicates. **(B)** Analysis of polar lipids of the indicated strains by bidimensional (2D)-layer chromatography (TLC) (2D-TLC). Phosphatidyl-myo-inositol dimannosides (Ac_1PIM_2 and Ac_2PIM_2, respectively); phosphatidyl-myo-inositol hexamannosides (Ac_xPIM_6); phosphatidylethanolamine (PE); diphosphatidylglycerol (DPG). Phospholipid (P). **(C)** Analysis of mycolic acid species in the indicated strains by TLC. **(D)** Analysis of PIDMs and TAGs by TLC. **(E)** Analysis of apolar lipids of the indicated strains by TLC. Diacylglycerol (DAG); free fatty acid (FF); free mycolic acid (FMA). **(F)** Analysis of apolar lipids of MEVs isolated from the indicated strains. Triacylglycerols (TAGs); phthiocerol dimycocerosates (PDIMs) **(G)** Analysis of polar lipids of MEVs isolated from the indicated strains. Phosphatidyl-myo-inositol dimannosides (Ac_1PIM_2 and Ac_2PIM_2, respectively); phosphatidyl-myo-inositol hexamannosides (Ac_xPIM_6); diphosphatidylglycerol (DPG).

Figure 7. Chemical and nanometric analysis of isolated cell walls shows higher amounts of PG in the absence of VirR. (A) Glycosyl composition analysis of isolated cell walls from the indicated strains. Acid hydrolysis prior to GC-MS analysis of isolated cell walls was performed to determine the total amounts of galactose (G), arabinose

(A), rhamnose (R), and N-acetylglucosamine (NAGc). The ratio between different sugars is shown to indicate: (i) the relative levels of arabinogalactan (A/G); (ii) the length of the AG polysaccharide chain (G/R); (iii) the amount of PG (NAGc/Rham). Individual measurements are shown from three biological replicates. Data are mean and standard errors. **P < 0.01 after applying a Tukey´s multiple comparison test. **(B)** Quantification of diaminopimelic acid (DAP) on isolated cell walls from the indicated strains. Data are mean and standard errors from three biological replicates; **** denotes P<0.0001, * denotes P=0.0119 after applying a Tukey´s multiple comparison test. **(C)** Atomic force microscopy high resolution images taken in liquid from the external surface of purified peptidoglycan from different samples, left to right: WT, *virR*^{mut}, *virR*^{mut}*-C*, the structure of external peptidoglycan layer shows a mesh with pores of different sizes, **(D)** Graph showing the pore diameter from n = 8 AFM images similar to **(C)** (each point represent an image) of different samples; black triangles: WT, blue circles: *virR*^{mut}, red squares: *virR*^{mut}*-C*. The pore diameter was calculated from the binary slice from each image containing the greatest number of pores, according to (Pasquina-Lemonche, 2024). **(E)** The number of pores per surface area from different samples; white triangles: WT, red circles: *virR*^{mut}, blue squares: *virR*^{mut}-C, this was calculated from the slice containing the maximum number of pores where the pore size was analyzed, following the method from (Pasquina-Lemonche, 2024). **(F)** Graph showing the peptidoglycan thickness manually measured using the 1D statistic tools from the open-source program Gwyddion (Nečas and Klapetek, 2012) from AFM images in air containing several fragments of cell wall, each point represents a different peptidoglycan fragment from a different cell. There were three samples analyzed: black WT n=23 peptidoglycan fragments, blue *virR*^{mut} n=36 and red *virR*^{mut}-C n=25. Statistics: D) Using a two-tailed t test with Welch's correction the statistical comparison are: (***) pWT- *virR*^{mut} = 4.1 10^{-4} with t = 6.1, df = 7.5, (**) p *virR*^{mut} - *virR*^{mut}-C = 0.007 with t = 3.2, df = 13.2, E) Using a two-tailed t test with Welch's correction the statistical comparison are: (****) pWT- *virR*^{mut} = 6.6 10-10 with t = 16.3, df = 12.7, (**) p *virR*^{mut} - *virR*^{mut} -C = 0.01 with t = 3.0, df = 13.2., F) Using a two-tailed t test with Welch's correction the statistical comparison are: (****) pWT- *virR*^{mut} = 2.8 10-18 with t = 17.8, df = 32.3, (****) *virR*^{mut} - *virR*^{mut} -C = 3.9 10-17 with t = 16.4, df = 31.8.

Figure 8. VirR interacts with Lcp1. (A) Blue-native PAGE analysis of recombinant VirR and Lcp1. The molecular mass of markers in kDa are indicated on the left side of the gel. The size of the multimers of VirR and Lcp1 are indicated on the left side of the gel. **(B)** *Upper panel*. Representative image of a flotation assay of recombinant VirR alone or in combination with Lcp1 performed on an idioxanol density gradient. The

presence of VirR was detected in each fraction by dot-blot using murine polyclonal antibodies raised against VirR. Numbers indicate collected fractions from top (1) to bottom (11). *Lower panel*. Quantification of the dot-blot by measuring the pixel intensity of the dots using ImageJ. Data are mean and standard error of three independent experiments. **(C)** Bipartite split-GFP experiment using *M. smegmatis* D2 expressing plasmids depicted in (**Fig S9A**), including VirR, VirRsol(Δ1-41), $CtpC_N$, Rv3484, Rv3267 (Lcp1), Rv0822, $Rv3484_{LytR_C}$, $Rv3267_{LytR_C}$ and $Rv0822_{LytR_C}$. Bacteria were grown in complete 7H9. Fluorescence was recorded by epifluorescence microscopy. The experiment was performed one time.

Supplementary Tables

Supplementary Table S1. Plasmids and primers used in this study.

Construction / DNA fragment used	Template	Primers	Sequence 5'-3'
pGMCS-P1-*virR*-Lk2-GFP11-*ctpC*(1-85)-Lk15-GFP(1-10)			
P1	pGMCS-TetR-P1-*pacL1*$_{Flag}$- P$_{pacL1}$-*ctpC*$_{His}$ (Boudehen *et al*. 2022)	Inf-B2-P1-Fw	CAAAGTGGAGCGATACTCGACATCGGATCGTCGGCACCGTCAC
		Inf-P1-Left	GAAATGATGTATGCCGTGCTGGTC
pGMCS backbone	pGMCS-P$_{pacL}$-*pacL1*-Lk2-GFP11-*ctpC*(1-85)-Lk15-GFP(1-10) (Boudehen *et al*. 2022)	ctpC-B2-Left	GTCGAGTATCGCTCCACTTTG
		Rv3269-P1-Fus-Fw	CAGCACGGCATACATCATTTCGGAAGAAAGGTACAGGCAATGG
pGMCS-P1-*virR*-Lk2-GFP11-*ctpC*(1-85)-Lk15-GFP(1-10)			
virR	*M. tuberculosis* H37Rv chromosomal DNA	If-AmL1-VirR	AAGGTACAGGCAATGgtgctggttacagtgggctcg
		If-Lk2-VirR-Rv	ACCGGATCCTTCCAGgccggtcaccacgacgatg
pGMCS backbone	pGMCS-P1-*pacL1*-Lk2-GFP11-*ctpC*(1-85)-Lk15-GFP(1-10)	Lk2-Right	CTGGAAGGATCCGGTGGCGG
		pGMC 3269 Am Left	CATTGCCTGTACCTTTCTTCC
pGMCS-P1-*virRsol*-Lk2-GFP11-*ctpC*(1-85)-Lk15-GFP(1-10)			
virRsol	*M. tuberculosis* H37Rv chromosomal DNA	If-AmL1-VirRsol	AAGGTACAGGCAATGctgggttcgtctccgaactccg
		If-Lk2-VirR-Rv	ACCGGATCCTTCCAGgccggtcaccacgacgatg
pGMCS backbone	pGMCS-P1-*pacL1*-Lk2-GFP11-*ctpC*(1-85)-Lk15-GFP(1-10)	Lk2-Right	CTGGAAGGATCCGGTGGCGG
		pGMC 3269 Am Left	CATTGCCTGTACCTTTCTTCC
pGMCS-P1-*virR*-Lk2-GFP11-*virR*-Lk15-GFP(1-10)			
virR	*M. tuberculosis* H37Rv chromosomal DNA	If-AmMBD-VirR	GAGCGCCTCGCCATGgtgctggttacagtgggctcg
		If-L15-VirR-Rv	AGACAGCCCTGGACCgccggtcaccacgacgatg
pGMCS backbone	pGMCS-P1-*virR*-Lk2-GFP11-*ctpC*(1-85)-Lk15-GFP(1-10)	Flex15-Right	GGTCCAGGGCTGTCTGGCC
		ctpC-Am-left2	CATGGCGAGGCGCTCAAG
pGMCS-P1-*virRsol*-Lk2-GFP11-*virRsol*-Lk15-GFP(1-10)			
virRsol	*M. tuberculosis* H37Rv chromosomal DNA	If-AmMBD-VirRsol	GAGCGCCTCGCCATGctgggttcgtctccgaactccg
		If-L15-VirR-Rv	AGACAGCCCTGGACCgccggtcaccacgacgatg

pGMCS backbone	pGMCS-P1-*virRsol*-Lk2-GFP11-*ctpC*(1-85)-Lk15-GFP(1-10)	Flex15-Right	GGTCCAGGGCTGTCTGGCC
		ctpC-Am-left2	CATGGCGAGGCGCTCAAG
pGMCS-P1-*virRsol*-Lk2-GFP11-*rv0822c*(LytR_C)-Lk15-GFP(1-10)			
Rv0822c(LytR_C)	*M. tuberculosis* H37Rv chromosomal DNA	If-AmMBD-0822cD	GAGCGCCTCGCCATGgagattcagcaccagcaggttacgacg
		If-L15-0822cD-Rv	AGACAGCCCTGGACCgcggcttatctgcacgctgacg
pGMCS backbone	pGMCS-P1-*virRsol*-Lk2-GFP11-*ctpC*(1-85)-Lk15-GFP(1-10)	Flex15-Right	GGTCCAGGGCTGTCTGGCC
		ctpC-Am-left2	CATGGCGAGGCGCTCAAG
pGMCS-P1-*virRsol*-Lk2-GFP11-*rv3267*(LytR_C)-Lk15-GFP(1-10)			
Rv3267(LytR_C)	*M. tuberculosis* H37Rv chromosomal DNA	If-AmMBD-3267D	GAGCGCCTCGCCATGcccgccaagaccacggcc
		If-L15-3267D-Rv	AGACAGCCCTGGACCcagcccggagcccggac
pGMCS backbone	pGMCS-P1-*virRsol*-Lk2-GFP11-*ctpC*(1-85)-Lk15-GFP(1-10)	Flex15-Right	GGTCCAGGGCTGTCTGGCC
		ctpC-Am-left2	CATGGCGAGGCGCTCAAG
pGMCS-P1-*virRsol*-Lk2-GFP11-*rv3484*(LytR_C)-Lk15-GFP(1-10)			
Rv3484(LytR_C)	*M. tuberculosis* H37Rv chromosomal DNA	If-AmMBD-3484D	GAGCGCCTCGCCATGgcggccgccaaacctaacc
		If-L15-3484D-Rv	AGACAGCCCTGGACCggtatccaccgtcacacggatg
pGMCS backbone	pGMCS-P1-*virRsol*-Lk2-GFP11-*ctpC*(1-85)-Lk15-GFP(1-10)	Flex15-Right	GGTCCAGGGCTGTCTGGCC
		ctpC-Am-left2	CATGGCGAGGCGCTCAAG
pGMCS-P1-*virRsol*-Lk2-GFP11-*rv0822c*(Cterm)-Lk15-GFP(1-10)			
Rv0822c(Cterm)	*M. tuberculosis* H37Rv chromosomal DNA	If-AmMBD-0822cD	GAGCGCCTCGCCATGgagattcagcaccagcaggttacgacg
		If-L15-0822c-Rv2	AGACAGCCCTGGACCctcgcaggtggtgtcggcg
pGMCS backbone	pGMCS-P1-*virRsol*-Lk2-GFP11-*ctpC*(1-85)-Lk15-GFP(1-10)	Flex15-Right	GGTCCAGGGCTGTCTGGCC
		ctpC-Am-left2	CATGGCGAGGCGCTCAAG
pGMCS-P1-*virRsol*-Lk2-GFP11-*rv3267*(Cterm)-Lk15-GFP(1-10)			
Rv0822c(Cterm)	*M. tuberculosis* H37Rv chromosomal DNA	If-AmMBD-3267D	GAGCGCCTCGCCATGgagattcagcaccagcaggttacgacg
		If-L15-3267-Rv2	AGACAGCCCTGGACCgttgatgcactccggcgcgtc
pGMCS backbone	pGMCS-P1-*virRsol*-Lk2-GFP11-*ctpC*(1-85)-Lk15-GFP(1-10)	Flex15-Right	GGTCCAGGGCTGTCTGGCC
		ctpC-Am-left2	CATGGCGAGGCGCTCAAG
pGMCS-P1-*virRsol*-Lk2-GFP11-*rv3484*(Cterm)-Lk15-GFP(1-10)			
Rv0822c(Cterm)	*M. tuberculosis* H37Rv chromosomal DNA	If-AmMBD-3267D	GAGCGCCTCGCCATGgagattcagcaccagcaggttacgacg
		If-L15-3484-Rv2	AGACAGCCCTGGACCgttcacgcagggcacgccg
pGMCS backbone	pGMCS-P1-*virRsol*-Lk2-GFP11-*ctpC*(1-85)-Lk15-GFP(1-10)	Flex15-Right	GGTCCAGGGCTGTCTGGCC
		ctpC-Am-left2	CATGGCGAGGCGCTCAAG
pGMCS-P1-*virRsol*-Lk2-GFP11-*rv0822c*-Lk15-GFP(1-10)			
Rv0822c	*M. tuberculosis* H37Rv chromosomal DNA	If-AmMBD-0822c	GAGCGCCTCGCCATGagtgacggcgagagcg
		If-L15-0822c-Rv	AGACAGCCCTGGACCctactcgcaggtggtgtcgg
pGMCS backbone	pGMCS-P1-*virRsol*-Lk2-GFP11-*ctpC*(1-85)-Lk15-GFP(1-10)	Flex15-Right	GGTCCAGGGCTGTCTGGCC
		ctpC-Am-left2	CATGGCGAGGCGCTCAAG
pGMCS-P1-*virRsol*-Lk2-GFP11-*rv3267*-Lk15-GFP(1-10)			
Rv3267(Cterm)	*M. tuberculosis*	If-AmMBD-	GAGCGCCTCGCCATGatgtctgcgcaacgtgtggtt

	H37Rv chromosomal DNA	3267	c
		lf-L15-3267-Rv	AGACAGCCCTGGACCtcagttgatgcactccggcgc
pGMCS backbone	pGMCS-P1-*virRsol*-Lk2-GFP11-*ctpC*(1-85)-Lk15-GFP(1-10)	Flex15-Right	GGTCCAGGGCTGTCTGGCC
		ctpC-Am-left2	CATGGCGAGGCGCTCAAG
pGMCS-P1-*virRsol*-Lk2-GFP11-*rv3484*-Lk15-GFP(1-10)			
Rv3484(Cterm)	*M. tuberculosis* H37Rv chromosomal DNA	lf-AmMBD-3484	GAGCGCCTCGCCATGgcgcgttctgagggc
		lf-L15-3484-Rv	AGACAGCCCTGGACCctagttcacgcagggcacgc
pGMCS backbone	pGMCS-P1-*virRsol*-Lk2-GFP11-*ctpC*(1-85)-Lk15-GFP(1-10)	Flex15-Right	GGTCCAGGGCTGTCTGGCC
		ctpC-Am-left2	CATGGCGAGGCGCTCAAG
CRISPRi mutants			
virR (158.1) c2	Rv0431	Rv0431crispr 1 F	GGGAGAGCAGCAGGAAGACGACGC
		Rv0431crispr 1 R	AAACGCGTCGTCTTCCTGCTGCTC
virR (42.2) c1	Rv0431	Rv0431crispr 2 F	GGGAACGAACCCAGTGCCTGCCAGA
		Rv0431crispr 2 R	AAACTCTGGCAGGCACTGGGTTCGT
cei (145.2) c1	Rv2700	Rv2700crispr 1 F	GGGAATCACGCAAGTCACCACCAC
		Rv2700crispr 1 R	AAACGTGGTGGTGACTTGCGTGAT
cei (47.3) c2	Rv2700	Rv2700crispr 2 F	GGGAGTCGGTGCCGAGCGCAAGGTCG
		Rv2700crispr 2 R	AAACGACCTTGCGCTCGGCACCGAC
VirR-Venus primers			
VirR-F			TCACTGGGGTGCTGGTTACAGTGGGCTC
VirR-R			ATAGGATCGCCGGTCACCACGACGAT
pMV-F			TGACCGGCGATCCTATGGTGAGCAAGGGC
pMV-R			ACCAGCACCCCAGTGAAAAGTTCTTCTCCTTTACTC

Supplementary Table 2. Gradient mobile phase composition for ion-pairing LC-MS/MS for the quantification of acetyl-CoA, methyl citrate and methylmalonyl-CoA.

Time (min)	Mobile Phase (%)	
	A	B
1	100	0
2	55	45
7	50	50
7.5	5	95
8	5	95
8.5	100	0
10	End	

A: water-methanol 07:3 (v/v) + 10mM tributylamine + 3mM acetic acid; B: pure methanol

Supplementary Table 3. Gradient mobile phase composition for ion-pairing LC-MS/MS for the quantification of pyruvate.

Time (min)	Mobile Phase (%)	
	A	B

1	5	95
6	95	5
7	95	5
8	5	95
10	End	

A: pure water; B: pure methanol

Supplementary Table 4. Quantifier MRM transitions and collision energies used for acety-CoA, methyl citrate, methylmalonyl-CoA and pyruvate.

Metabolite	**Precursor ion $[M-H]^-$ (m/z)**	**Product ion (m/z)**	**Collision energy (eV)**
Acetyl-CoA	808.00	407.95	41
Methyl citrate	204.90	125.10	13
Methylmalonyl-CoA	432.60	410.50	10
Pyruvate	87.20	43.10	13

Supplementary figures

Fig S1. Diversity of *Mtb* LCP proteins. (**A**) Domain structure of LCP proteins in *Mtb*. Proteins are organized according to the presence of (i) both LCP (green) and LytR_C (slight orange) terminal domain (Rv3267, Rv3484 and Rv0822); (ii) the solo LytR_C domain (VirR and Rv2700); and the solo LCP domain (Rv3840). Additional information is provided for *Mtb* mutants in the indicated genes. (**B**) Phylogenetic analysis of LCP proteins in Mycobacteria (*M. tuberculosis, M. smegmatis, M. marinum and M. leprae*). The unrooted tree includes seven separate clusters for proteins with both LCP and LytR_C terminal domains (CpsA1, CpsA2 and CpsA3); with the solo LytR_C terminal domain (Solo_LytRC1 and Solo_LytRC2); with the solo LCP domain; and a separate cluster including the characterized LCP proteins from *S. pneumonia* and *S. aureus*. Note the clustering of one of the *M. smegmatis* LCP proteins with this group. VirR is highlighted in blue.

Fig S2. The enhanced vesiculation phenotype of *virR^{mut}* occurs in the absence of cell lysis. **(A)** Nanoparticle tracking analysis (NTA) of EV preparations derived from WT and the indicated strains showing number of particles per cm^3 determined by Zeta View NTA in three independent EV preparations. Data are presented as mean ± SEM. *P ≤ 0.05 (One-way ANOVA with Tukey's multiple comparisons test). **(B)** Cell lysis control of *virR^{mut}*. Shown are immunoblots of cell lysates and culture supernatants (SN) for the indicated strains. The cytoplasmic protein IdeR was detected in cell lysates but not in culture supernatants confirming cell integrity, while the secreted protein Ag85b was readily detected in the culture supernatants. **(C)** Cell lysis control of *Mtb* submitted to conditions that alter permeability. Arrows indicate the size of the proteins of interest detected by immunoblot.

Fig S3. Expression patterns of proteins contributing to enrichments of terms related to translation.

Fig S4. Expression patterns of proteins contributing to enrichments of terms related to nucleotide (A), amino-acids (B), oligosaccharides (C), and glycogen (D) metabolism, differentially expressed in both directions.

Fig S5. Expression patterns of the 39 genes in the DosR regulon that are simultaneously upregulated in cholesterol-enriched medium and down-regulated in *virR*^{mut} ((Brzostek et al., 2009)**, GSE175812).**

Fig S6. Additional AFM data. (A-C) (i) Atomic force microscopy images taken in liquid from a big area showing the sample heterogeneity overview with various peptidoglycan fragments of the following samples: **(A)** WT, **(B)** *virR*^{mut}, **(C)**, *virR*^{mut}-C. **(ii)** Atomic force microscopy images zoom in one individual peptidoglycan fragment corresponding to one cell from different samples: **(A)** WT, **(B)** *virR*^{mut} showing the background (Backg.), the external surface (Ext) the internal (Int), **(C)**, *virR*^{mut}-C, white square showing the size of the zoom images shown in Figure 5 from the external surface of the cells. **(D)** Curve of grey points showing 255 slices of one AFM image taken using a FIJI macro, in the x axis and the total number of pores in the y axis, the red line is a Gaussian fitted to the curve and the maximum of the Gaussian is marked with a dash red line showing slice 140 in this example corresponding to the slice of the image with the maximum number of pores. **(E)** Binary slice number 140 from the original AFM image showing the pores in white and the material represented in black. **(F)** The pores from 'E' were analyzed using the FIJI macros where each pore area was measured and plotted in the x axis against the cumulative fraction of total pore area in the y axis as shown in the curve by blue dots. The red dot marks the most likely pore area which corresponds to the half of the cumulative fraction of the total pore area, this area was then used to obtain the pore diameter of the image. The same was repeated with the n = 8 images for each sample to compose the graphs 'D' and 'E' from Figure 7.

Fig S7. **Sensitivity to lysozyme of *virR*^{mut}.** **(A)** Analysis of the minimum inhibitory concentration (MIC) of lysozyme of the indicated strains by the resazurin method. **(B)** Growth of WT and *virR*^{mut} treated with 0 or 50 µg/ml lysozyme (Lys). Data represents the mean ± SEM of three independent cultures.

Fig S8. Localization of VirR by fluorescence microscopy. Fluorescence images of a *Mtb* strain expressing Venus-tagged VirR.

Fig S9. Split-GFP strategy. (A) *Upper panel*. Scheme of the plasmid used to test VirR interactions in vivo. *Lower panel*. Scheme of the potential molecular interaction between VirR and Lcp1 using split-GFP. **(B)** Gating strategy to analyze split-GFP flow cytometry data. Bacteria were first sorted based on size (FSC) and structure (SSC) to exclude debris (1). Then, aggregates were excluded based on FSC and SSC width (W) and eighth (H) (2,3). GFP signal was then analyzed *vs*. SSC (4) or mCherry, when relevant (5).

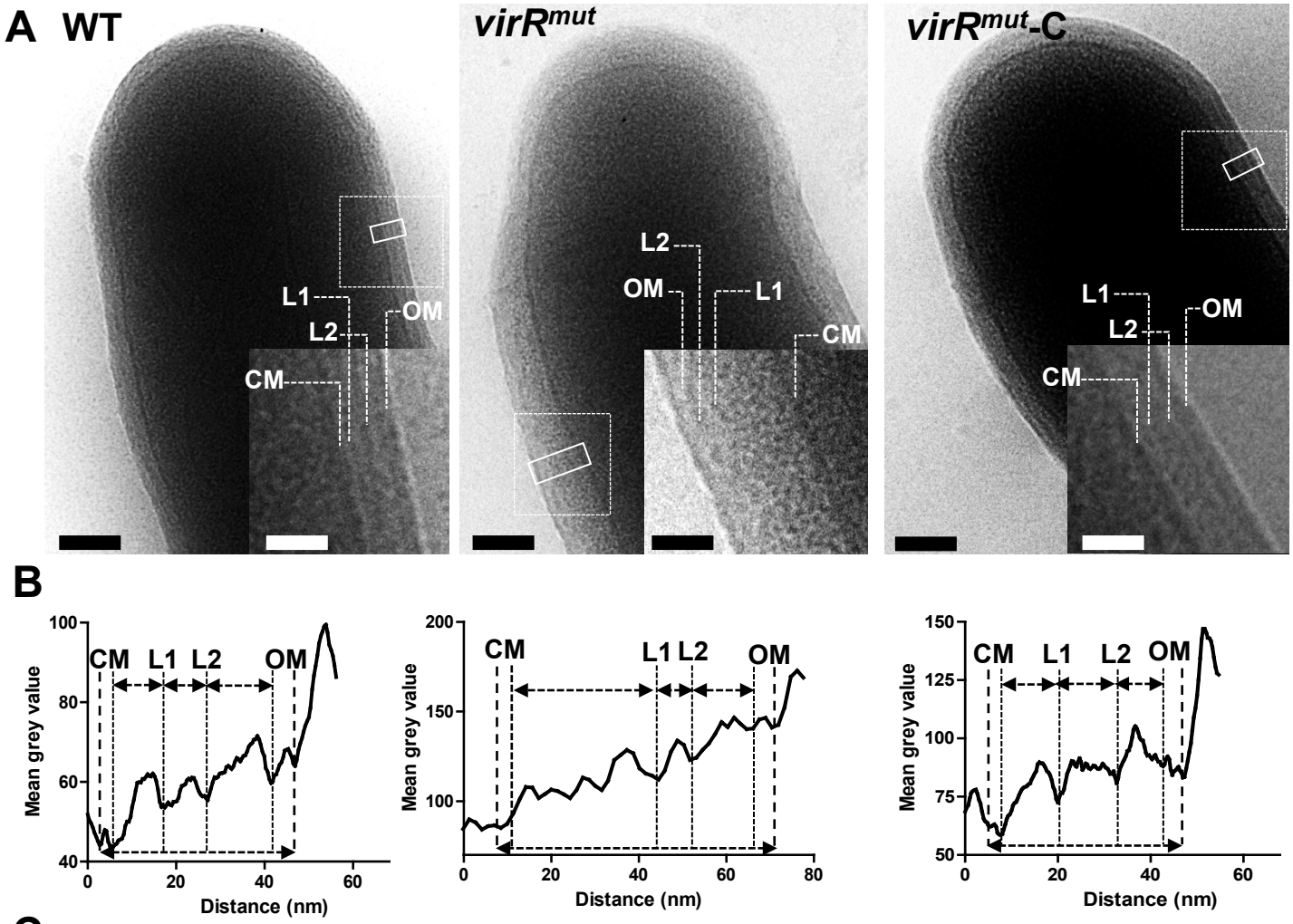

C

	CM	CM-OM	CM-L1	OM-L2	L1-L2	OM
WT	2.7±0.2	44.09±3.1	11.2±0.4	13.34±0.9	10.46±1.4	5.7±0.4
***virR*^{mut}**	5.4±0.7*	62.7±3.2*	31.36±3.2*	15.1±2.2	6.8±0.9*	6.1±0.3
***virR*^{mut}-C**	2.5±0.5	41.6±0.7	12.4±1.4	10.03±1.1	12.6±1.3	5±0.2

Figure 1

Figure 1. Ultrastructural changes in the cell envelope of *virR*-deficient mutant associated with increased vesiculation. (A) Cryo-electron micrographs of indicated Mtb strains grown in high iron MM. Closed line rectangles were used to calculate grey value profiles of cell envelopes using ImageJ. The dashed line insets within the main micrograph were magnified to show a detailed view of the cell surface. Scale bars are 100 nm in main micrographs and 50 nm in the insets. (B) Density profiles based on grey values of the cross sections marked by solid line rectangles in A. (C) Mean values and standard errors of distances in nm between main cell envelope layers measured in A and C. *$P < 0.05$ after applying a Tukey´s multiple comparison test. The number of cells analyzed varied from n = 20 (WT), n = 15 (virRmut) and n = 23 (virRmut-C). CM, cytoplasmic membrane; OM, outer membrane; L1, layer 1; L2, layer 2.

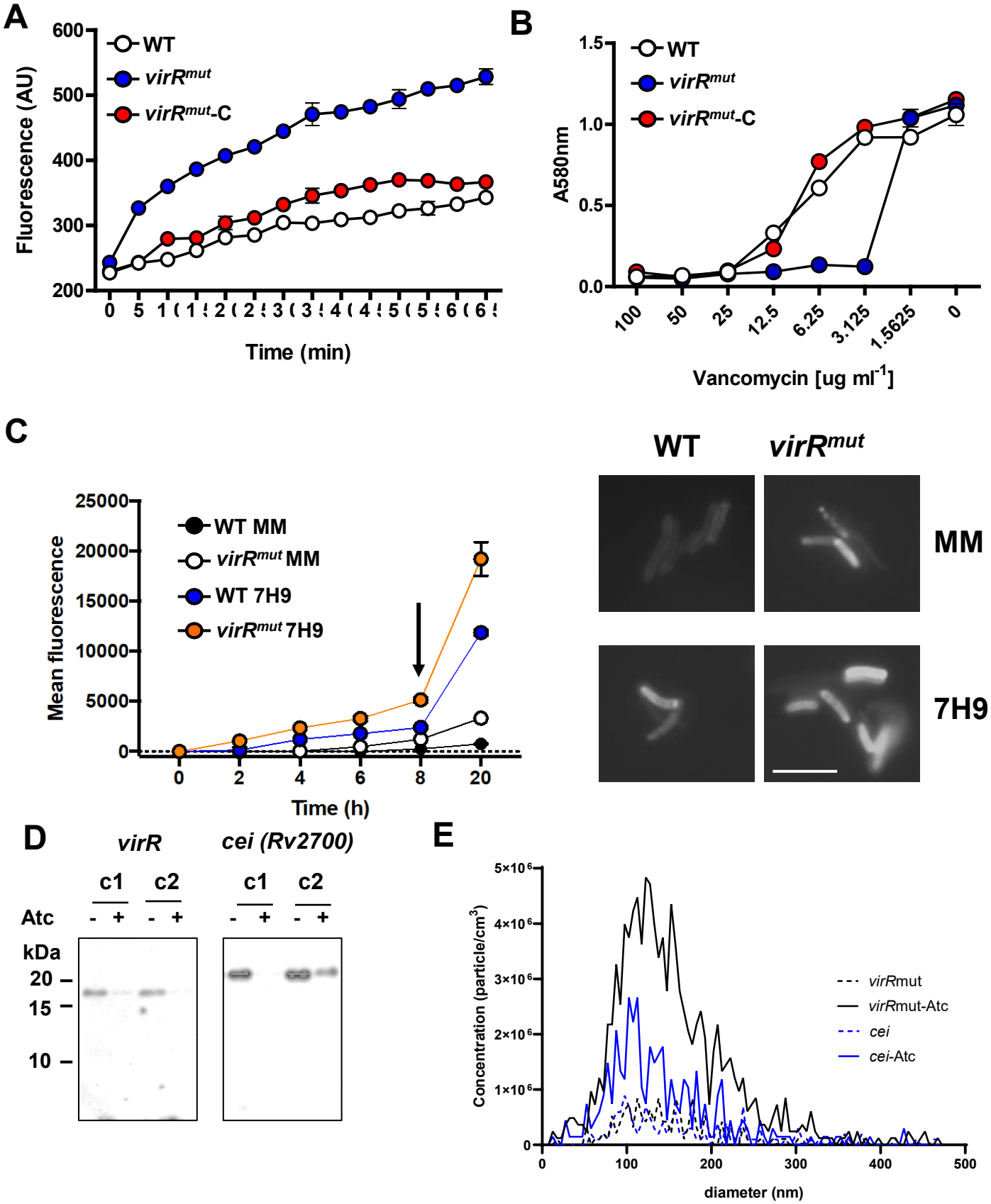
A
Fluorescence (AU)
600
500
400
300
200
WT
virRmut
virRmut-C
Time (min)
B
A580nm
1.5
1.0
0.5
0.0
WT
virRmut
virRmut-C
100
50
25
12.5
6.25
3.125
1.5625
0
Vancomycin [ug ml-1]
C
Mean fluorescence
25000
20000
15000
10000
5000
0
WT MM
virRmut MM
WT 7H9
virRmut 7H9
0
2
4
6
8
20
Time (h)
WT
virRmut
MM
7H9
D
virR
cei (Rv2700)
c1
c2
c1
c2
Atc
- + - +
- + - +
kDa
20
15
10
E
Concentration (particle/cm3)
5×10 6
4×10 6
3×10 6
2×10 6
1×10 6
0
virRmut
virRmut-Atc
cei
cei-Atc
0
100
200
300
400
500
diameter (nm)

Figure 2

Figure 2. Enhanced permeability and vesiculation are linked in the absence of LytR_C solo domain proteins in Mtb. (A) Uptake of ethidium bromide (EthBr) in the indicated strains, as measured by fluorescence at 590 nm for 65 min. Data are mean and standard deviation of three biological replicates. (B) Sensitivity of the indicated strains to different concentrations of vancomycin as measured by monitoring optical density at 580 nm (OD580) after 7 days. Data are mean and standard deviations of three biological replicated. Errors bars not shown are smaller than symbols. (C) Time course of the incorporation of FDAAs on the indicated strains in both 7H9 and MM as measured by fluorescence. Representative images of both WT and virRmut strains in either 7H9 or MM at 8h after the addition of the FDAA. Data are mean and standard deviations of three biological replicates. The arrow indicates the time at which images were taken. Errors bar not shown are smaller than symbols. (D) immunoblot analysis of cell lysates of two independent conditional mutants (c1 and c2) for virR and cei for the presence of VirR and Cei proteins in cultures incubated with and without anhydrotetracycline (ATc). (E) Nanoparticle tracking analysis (NTA) of EV preparations derived from virR and cei conditional mutants (c2 (virR) and c1 (cei)) obtained from cultures with and without ATc showing number of particles per cm3 determined by Zeta View NTA in three independent EV preparations. Data are presented as mean ± SEM.

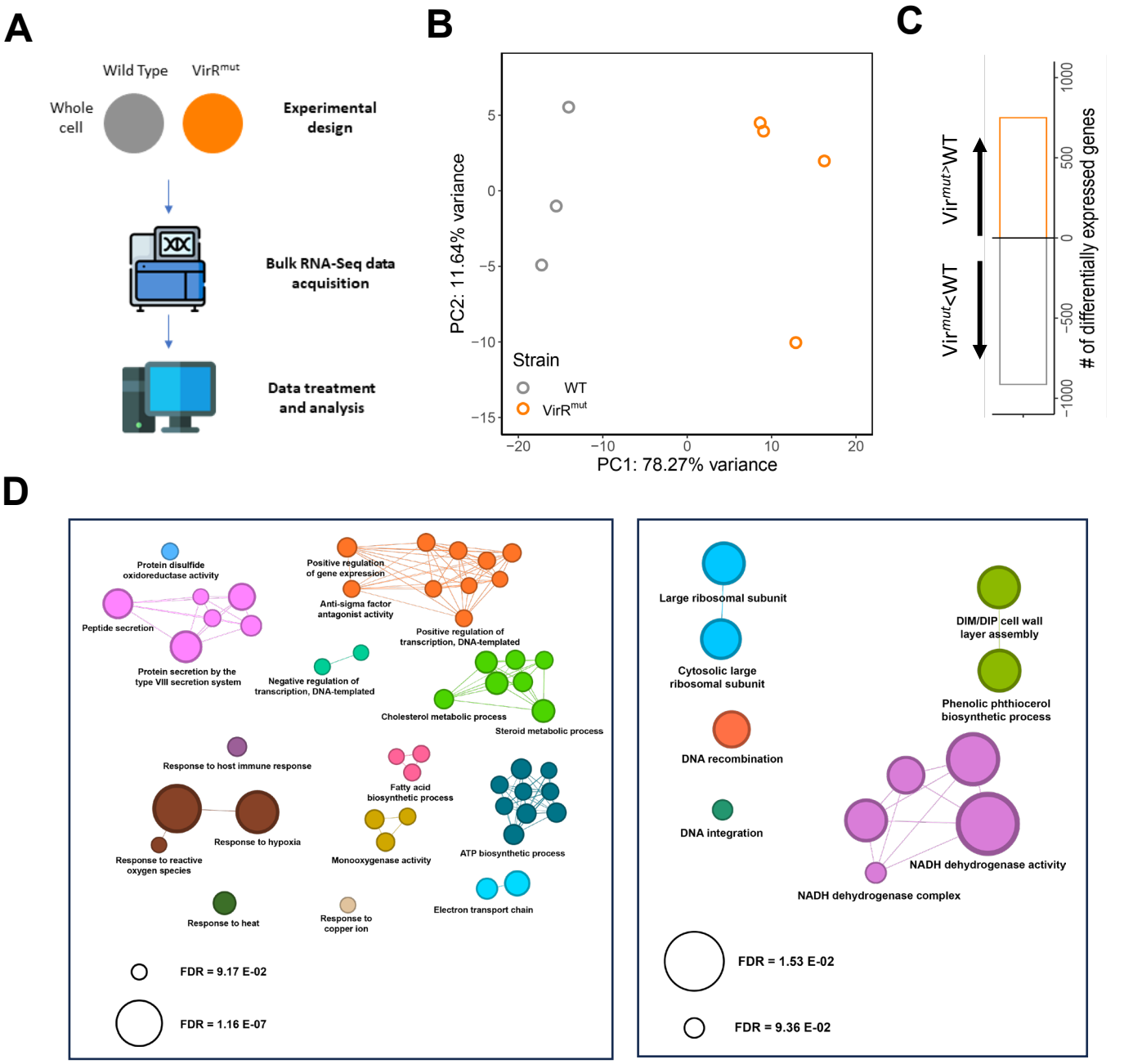
A
Wild Type
VirR^mut
Whole cell
Experimental design
Bulk RNA-Seq data acquisition
Data treatment and analysis
B
PC2: 11.64% variance
PC1: 78.27% variance
Strain
WT
VirR^mut
C
Vir^mut>WT
Vir^mut<WT
# of differentially expressed genes
D
Protein disulfide oxidoreductase activity
Peptide secretion
Protein secretion by the type VIII secretion system
Positive regulation of gene expression
Anti-sigma factor antagonist activity
Positive regulation of transcription, DNA-templated
Negative regulation of transcription, DNA-templated
Cholesterol metabolic process
Steroid metabolic process
Response to host immune response
Response to hypoxia
Response to reactive oxygen species
Fatty acid biosynthetic process
Monooxygenase activity
ATP biosynthetic process
Electron transport chain
Response to heat
Response to copper ion
FDR = 9.17 E-02
FDR = 1.16 E-07
Large ribosomal subunit
Cytosolic large ribosomal subunit
DNA recombination
DNA integration
DIM/DIP cell wall layer assembly
Phenolic phthiocerol biosynthetic process
NADH dehydrogenase activity
NADH dehydrogenase complex
FDR = 1.53 E-02
FDR = 9.36 E-02

Figure 3

Figure 3. Transcriptional profiling of virRmut showcases systemic alterations in cell wall architecture and metabolism. (A) Experiment design for RNA-seq analyses. RNA was extracted from whole cell extracts from 4 replicate cultures of each strain (WT and virRmut), and sequenced. Of these 8 samples, 7 passed quality control, (3 WT and 4 virRmut) and were subsequently analyzed. (B) PCA plot of the transcriptomics data. The loadings from the two first principal components are plotted. PC1 (X axis) significantly separates samples across strains (One tailed Mann Whitney test: PC1 in WT vs virRmut: p=2.86 e-02). (C) Number of differentially expressed genes between virRmut and WT. virRmut significantly affects expression of a total of 750+913=1663 genes, (Storey-Tibshirani FDR=5%), which represents 41.5% of all genes tested. (D) Gene Ontology (GO) enrichments of downregulated genes in virRmut (left) and upregulated ones (right). GO terms selected for testing included biological process and cell compartment labels containing N≥10 genes, between levels 4-6 of the ontology tree. In this representation, each node in the networks represents a significantly enriched term (terms selected for visualization with FDR=10% and enrichment odds-ratio>2), nodes' size is proportional to the enrichment significance, and links between terms are added wherever the sets of genes contributing to the enrichments in a connected pair show an intersection larger than 50% of the smallest of the gene sets involved in the pair (see Methods for further details, and supplementary table S2 for an extended list of all the enrichments found).

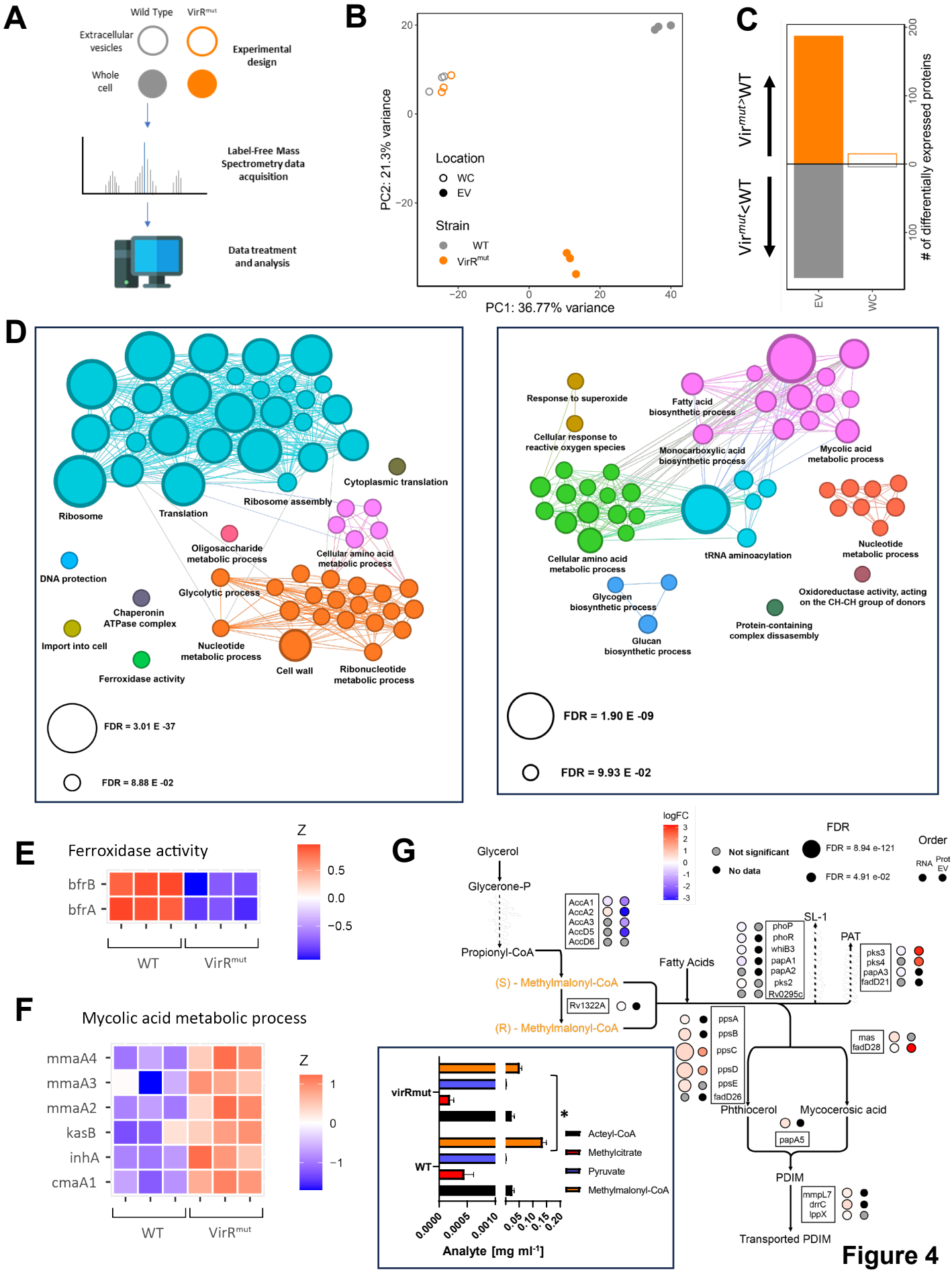
A
Wild Type
VirR^mut
Extracellular vesicles
Whole cell
Experimental design
Label-Free Mass Spectrometry data acquisition
Data treatment and analysis
B
PC2: 21.3% variance
PC1: 36.77% variance
Location
WC
EV
Strain
WT
VirR^mut
C
Vir^mut>WT
Vir^mut<WT
# of differentially expressed proteins
EV
WC
D
Ribosome
Translation
Ribosome assembly
Cytoplasmic translation
Oligosaccharide metabolic process
Cellular amino acid metabolic process
DNA protection
Glycolytic process
Chaperonin ATPase complex
Import into cell
Nucleotide metabolic process
Cell wall
Ribonucleotide metabolic process
Ferroxidase activity
FDR = 3.01 E -37
FDR = 8.88 E -02
Response to superoxide
Fatty acid biosynthetic process
Cellular response to reactive oxygen species
Monocarboxylic acid biosynthetic process
Mycolic acid metabolic process
Nucleotide metabolic process
Cellular amino acid metabolic process
tRNA aminoacylation
Oxidoreductase activity, acting on the CH-CH group of donors
Glycogen biosynthetic process
Protein-containing complex dissassembly
Glucan biosynthetic process
FDR = 1.90 E -09
FDR = 9.93 E -02
E
Ferroxidase activity
bfrB
bfrA
WT
VirR^mut
Z
0.5
0.0
−0.5
F
Mycolic acid metabolic process
mmaA4
mmaA3
mmaA2
kasB
inhA
cmaA1
WT
VirR^mut
Z
1
0
−1
G
Glycerol
Glycerone-P
Propionyl-CoA
(S) - Methylmalonyl-CoA
(R) - Methylmalonyl-CoA
Rv1322A
AccA1
AccA2
AccA3
AccD5
AccD6
logFC
Not significant
No data
FDR
FDR = 8.94 e-121
FDR = 4.91 e-02
Order
RNA
Prot
EV
Fatty Acids
phoP
phoR
whiB3
papA1
papA2
pks2
Rv0295c
SL-1
PAT
pks3
pks4
papA3
fadD21
ppsA
ppsB
ppsC
ppsD
ppsE
fadD26
mas
fadD28
Phthiocerol
Mycocerosic acid
papA5
PDIM
mmpL7
drrC
lppX
Transported PDIM
virRmut
WT
Acteyl-CoA
Methylcitrate
Pyruvate
Methylmalonyl-CoA
Analyte [mg ml-1]
Figure 4

Figure 4. virR regulates the protein content of EVs in Mtb. (A). Experiment design for proteomics analyses. label-free mass spectrometry data was retrieved for three replicates of H37RV and virRmut. For each strain, in turn, data corresponding to proteins extracted from either whole-cell extracts (WC) and EVs was produced, totaling 12 samples (2 strains times 2 cell compartments times 3 replicates). (B) PCA plot of the proteomics data. The loadings from the two first principal components are plotted. PC1 (X axis) significantly separates samples across cell-compartments (One-tailed Mann Withney test: PC1 in EVs vs WC: p= 1.08 e-03), while PC2 separates samples from EVs in virRmut from the rest of samples (one-tailed Mann Withney test: PC2 in virRmut in EV vs all other samples: p=4.55 e-03), indicating a differential peptidic cargo in the vesicles of virRmut. (C) Bar plots of differentially expressed proteins found between strains in in whole cell extracts (left, 19 differentially expressed proteins at 5% FDR), and extracellular vesicles (right, 353 differentially expressed proteins at 5% FDR). (D) Gene Ontology enrichments of the downregulated proteins in the VirR mutant strain (left) and the upregulated ones (Right), at the EV location. GO terms selected for testing included biological process and cell compartment labels containing N≥3 genes, between levels 4-6 of the ontology tree. As in figure 3D, terms selected for visualization with FDR=10% and enrichment odds-ratio>2, nodes' size is proportional to the enrichment significance, and links between terms are added wherever the sets of proteins contributing to the enrichments in a connected pair shows an intersection larger than 50% of the smallest of the gene sets involved in the pair (see Methods for further details, and supplementary table S2 for an extended list of all the enrichments found). (E) Expression patterns of bacterioferritin proteins in the extracellular vesicles of WT and virRmut. (F) Expression patterns of proteins contributing to enrichments of terms related to mycolic acids biosynthesis. (G) Bottom left: Concentrations of key metabolites in the propionyl-coA detoxification routes. Right: Metabolic pathway of the propionyl-coA detoxification route through the methyl-malonyl route, along with the differential expression statistics between the WT and virRmut strains observed at transcriptomic and proteomic levels for the main enzymes involved. The framed plot represents the quantification of selected metabolites by mass spectrometry.

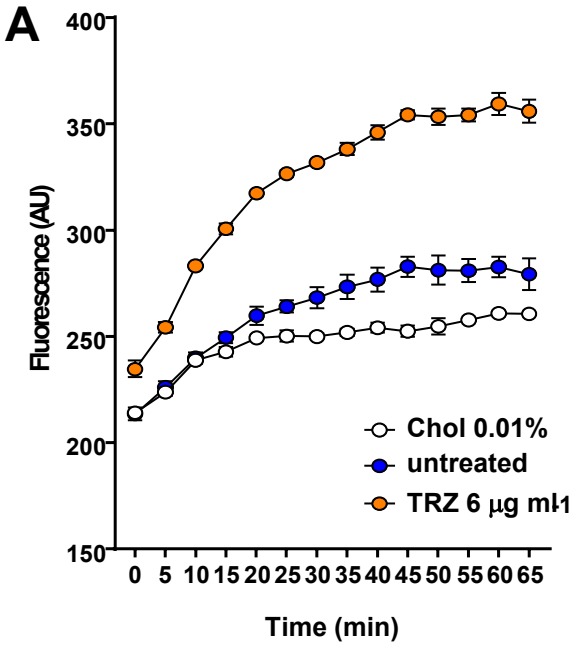
A
Fluorescence (AU)
Time (min)
Chol 0.01%
untreated
TRZ 6 µg ml-1

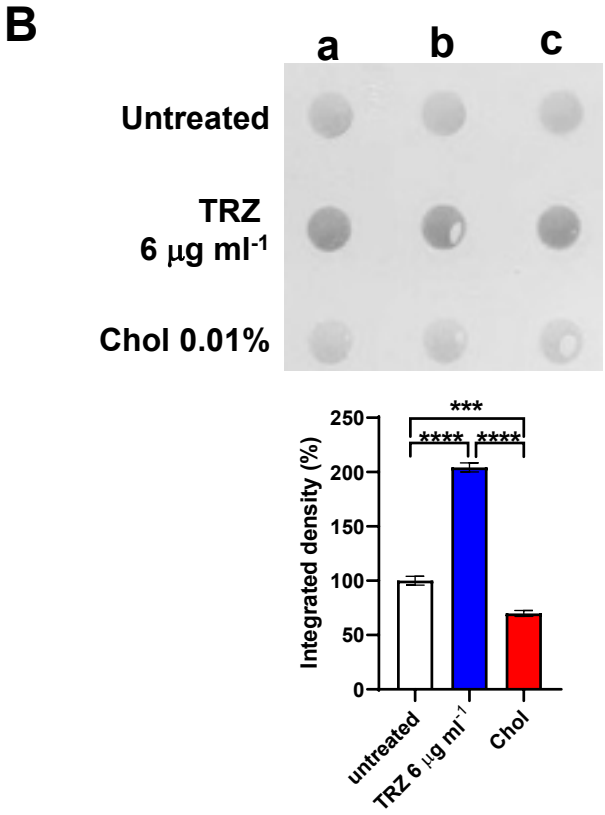
B
a
b
c
Untreated
TRZ
6 µg ml-1
Chol 0.01%
Integrated density (%)
untreated
TRZ 6 µg ml-1
Chol

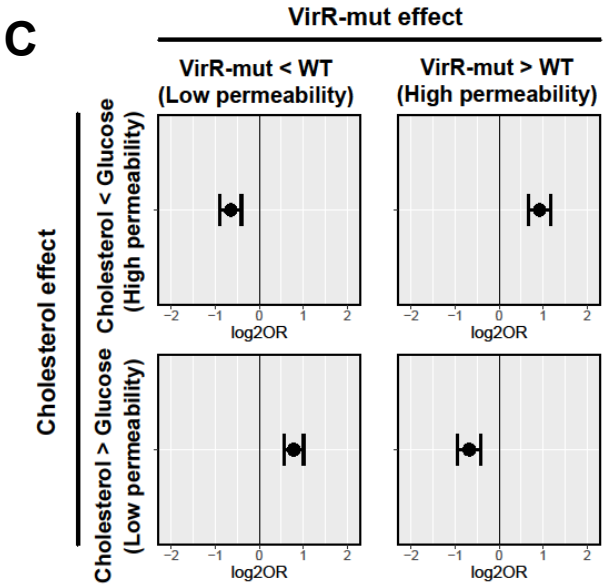
C
VirR-mut effect
VirR-mut < WT
(Low permeability)
VirR-mut > WT
(High permeability)
Cholesterol effect
Cholesterol < Glucose
(High permeability)
Cholesterol > Glucose
(Low permeability)
log2OR

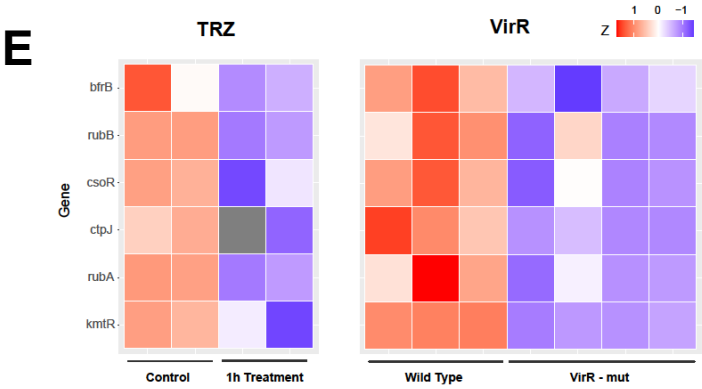
E
TRZ
VirR
Gene
bfrB
rubB
csoR
ctpJ
rubA
kmtR
Control
1h Treatment
Wild Type
VirR - mut

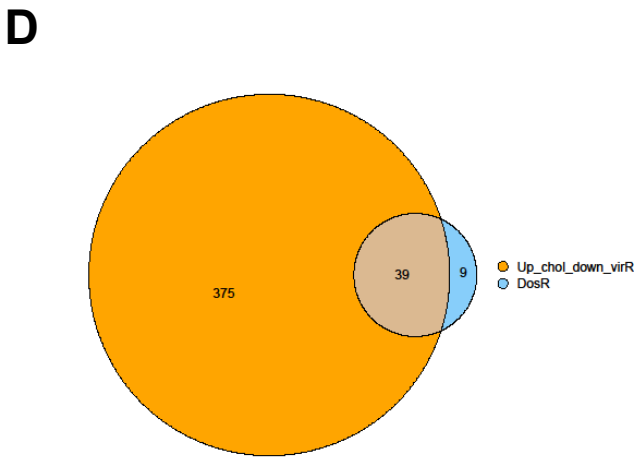
D
375
39
9
Up_chol_down_virR
DosR

Figure 5

Figure 5. Cell permeability is a major driver of vesicle production in Mtb. (A) Time course of the uptake of ethidium bromide (EthBr) by Mtb grown in the indicated conditions, as measured by fluorescence at 590 nm for 65 min. Data are mean and standard deviation of three biological replicates. (B) Dot-blot analysis of released EVs in supernatants from Mtb cultures submitted to the indicated conditions. The loading volume was normalized according to CFUs. The graph below represents the quantification of the dotblot using ImageJ. The integrated cell density was normalized to WT values. Data are mean and standard errors from the three biological replicates; **** denotes P<0.0001, *** denotes P=0.0028 after applying a Tukey´s multiple comparison test. (C) Enrichment odds ratios for Fisher exact tests comparing sets of genes up, and down regulated, respectively, in 1)cholesterol-supplemented medium vs. glucose-supplemented medium ((Pawełczyk et al., 2021), GEO accession GSE175812); and 2) virRmut vs WT. (D) Euler diagram showing that 39 out of 48 genes in the DosR regulon are simultaneously repressed in virRmut vs WT, and upregulated in cholesterol vs. glucose enriched medium cultures, suggesting a common activation of the regulon in conditions of low permeability (see also Fig S5). (E) Expression patterns in response to TRZ (1h) and in virRmut for key genes involved in metal signaling, metabolism and homeostasis.

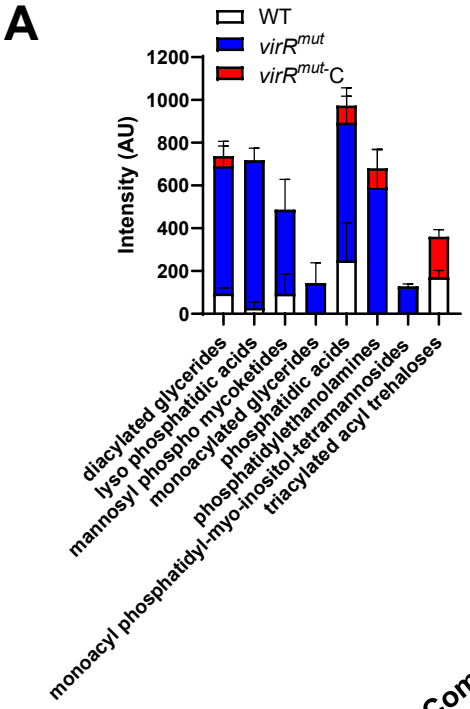
A
WT
virRmut
virRmut-C
Intensity (AU)
1200
1000
800
600
400
200
0
diacylated glycerides
lyso phosphatidic acids
mannosyl phospho mycoketides
monoacylated glycerides
phosphatidic acids
phosphatidylethanolamines
monoacyl phosphatidyl-myo-inositol-tetramannosides
triacylated acyl trehaloses

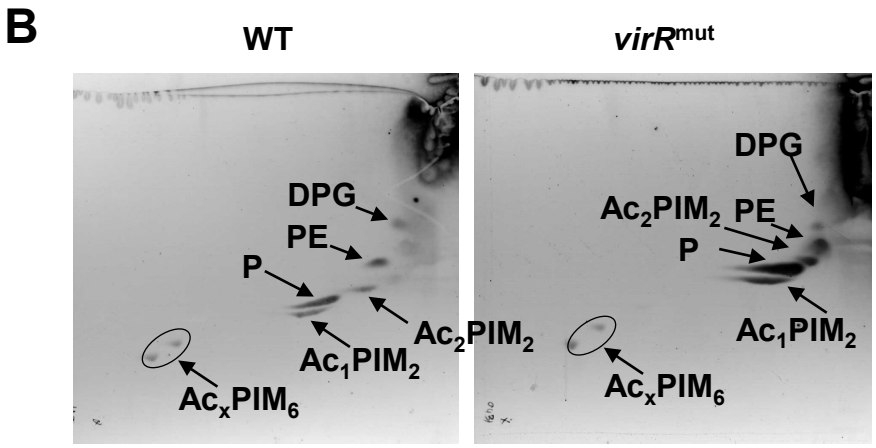
B
WT
virRmut
DPG
PE
P
Ac2PIM2
Ac1PIM2
AcxPIM6
DPG
Ac2PIM2
PE
P
Ac1PIM2
AcxPIM6

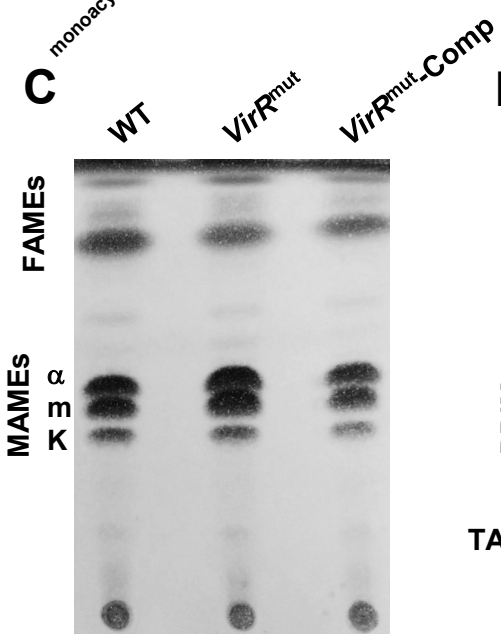
C
WT
VirRmut
VirRmut-Comp
FAMEs
MAMEs
α
m
K

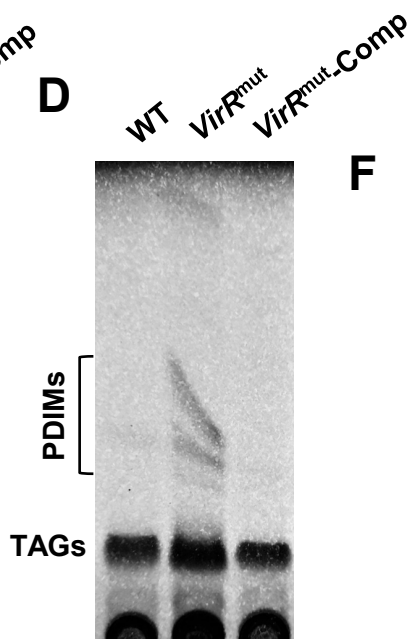
D
WT
VirRmut
VirRmut-Comp
PDIMs
TAGs

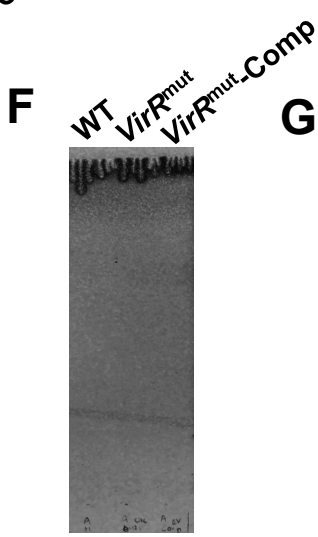
F
WT
VirRmut
VirRmut-Comp

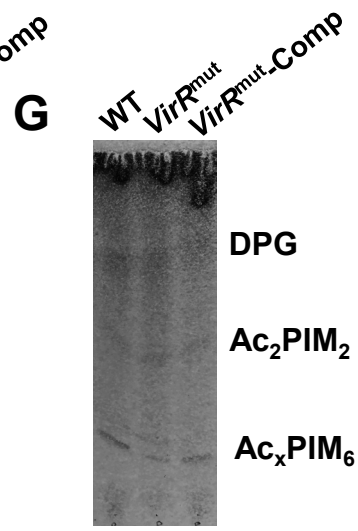
G
WT
VirRmut
VirRmut-Comp
DPG
Ac2PIM2
AcxPIM6

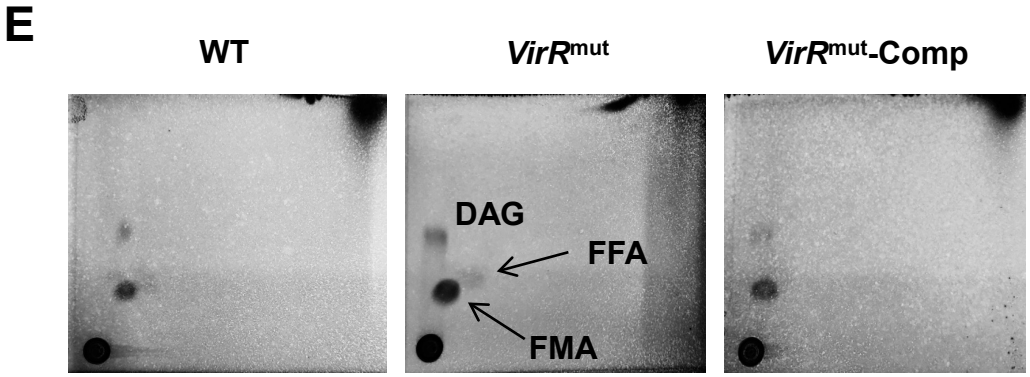
E
WT
VirRmut
VirRmut-Comp
DAG
FFA
FMA

Figure 6

Figure 6. Lipidomic analysis of cell envelope and EVs from virRmut. (A) Comparative total lipid analysis of the indicated strains by nano-LC-MS. Lipid species with an abundance higher than 0.5% are shown. Data indicates mean and standard error from three biological replicates. (B) Analysis of polar lipids of the indicated strains by bidimensional (2D)-layer chromatography (TLC) (2D-TLC). Phosphatidyl-myo-inositol dimannosides (Ac1PIM2 and Ac2PIM2, respectively); phosphatidyl-myo-inositol hexamannosides (AcxPIM6); phosphatidylethanolamine (PE); diphosphatidylglycerol (DPG). Phospholipid (P). (C) Analysis of mycolic acid species in the indicated strains by TLC. (D) Analysis of PIDMs and TAGs by TLC. (E) Analysis of apolar lipids of the indicated strains by TLC. Diacylglycerol (DAG); free fatty acid (FF); free mycolic acid (FMA). (F) Analysis of apolar lipids of MEVs isolated from the indicated strains. Triacylglycerols (TAGs); phthiocerol dimycocerosates (PDIMs) (G) Analysis of polar lipids of MEVs isolated from the indicated strains. Phosphatidyl-myo-inositol dimannosides (Ac1PIM2 and Ac2PIM2, respectively); phosphatidyl-myo-inositol hexamannosides (AcxPIM6); diphosphatidylglycerol (DPG).

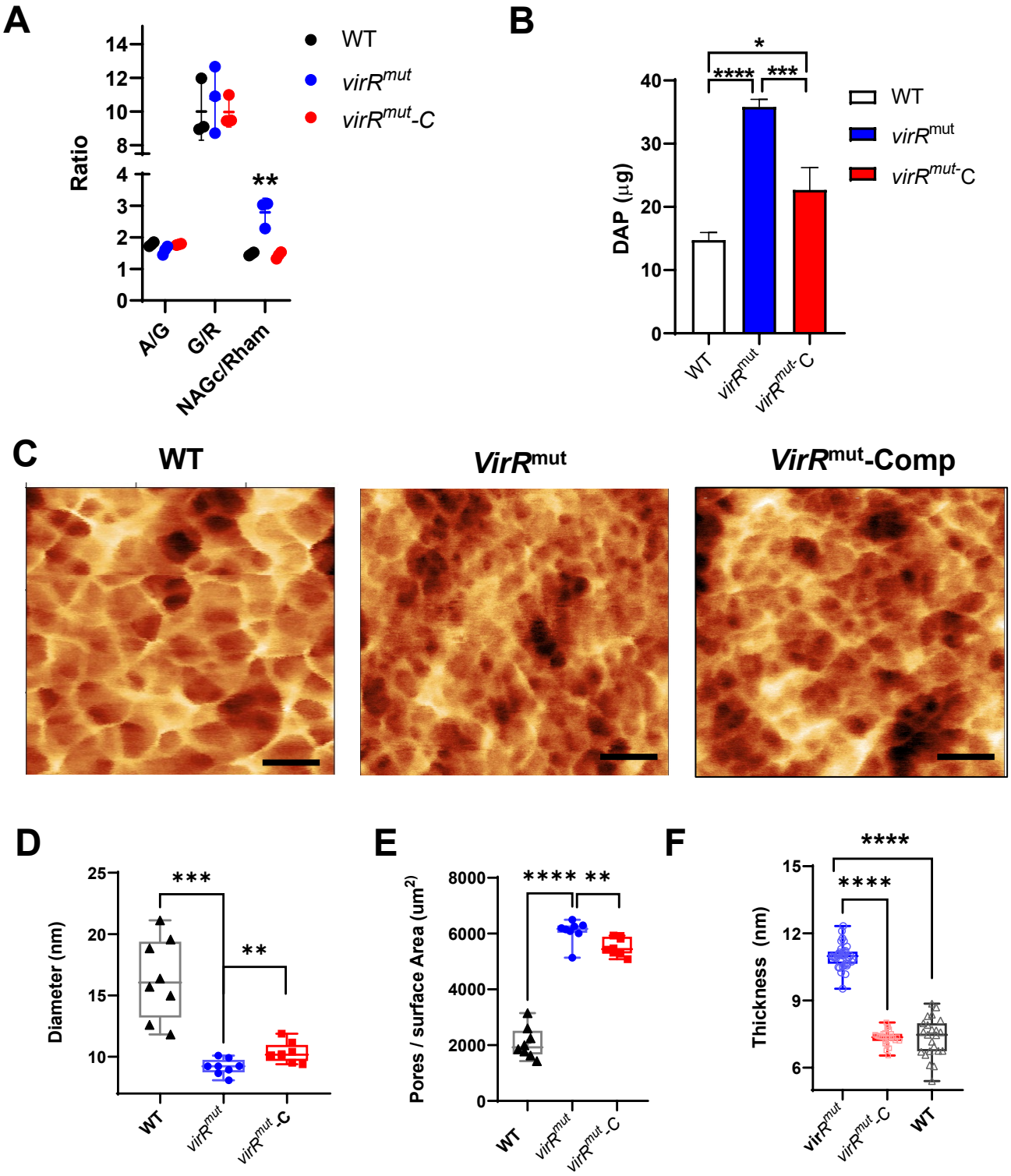
A
Ratio
WT
virRmut
virRmut-C
**
A/G
G/R
NAGc/Rham
B
DAP (µg)
*
****
***
WT
virRmut
virRmut-C
C
WT
VirRmut
VirRmut-Comp
D
Diameter (nm)
***
**
E
Pores / surface Area (um2)
**** **
F
Thickness (nm)
****
****

Figure 7

Figure 7. Chemical and nanometric analysis of isolated cell walls shows higher amounts of PG in the absence of VirR. (A) Glycosyl composition analysis of isolated cell walls from the indicated strains. Acid hydrolysis prior to GC-MS analysis of isolated cell walls was performed to determine the total amounts of galactose (G), arabinose (A), rhamnose (R), and N-acetylglucosamine (NAGc). The ratio between different sugars is shown to indicate: (i) the relative levels of arabinogalactan (A/G); (ii) the length of the AG polysaccharide chain (G/R); (iii) the amount of PG (NAGc/Rham). Individual measurements are shown from three biological replicates. Data are mean and standard errors. **P < 0.01 after applying a Tukey´s multiple comparison test. (B) Quantification of diaminopimelic acid (DAP) on isolated cell walls from the indicated strains. Data are mean and standard errors from three biological replicates; **** denotes P<0.0001, * denotes P=0.0119 after applying a Tukey´s multiple comparison test. (C) Atomic force microscopy high resolution images taken in liquid from the external surface of purified peptidoglycan from different samples, left to right: WT, virRmut, virRmut-C, the structure of external peptidoglycan layer shows a mesh with pores of different sizes, (D) Graph showing the pore diameter from n = 8 AFM images similar to (C) (each point represent an image) of different samples; black triangles: WT, blue circles: virRmut, red squares: virRmut-C. The pore diameter was calculated from the binary slice from each image containing the greatest number of pores, according to (Pasquina-Lemonche, 2024). (E) The number of pores per surface area from different samples; white triangles: WT, red circles: virRmut, blue squares: virRmut-C, this was calculated from the slice containing the maximum number of pores where the pore size was analyzed, following the method from (Pasquina-Lemonche, 2024). (F) Graph showing the peptidoglycan thickness manually measured using the 1D statistic tools from the open-source program Gwyddion (Nečas and Klapetek, 2012) from AFM images in air containing several fragments of cell wall, each point represents a different peptidoglycan fragment from a different cell. There were three samples analyzed: black WT n=23 peptidoglycan fragments, blue virRmut n=36 and red virRmut-C n=25. Statistics: D) Using a two-tailed t test with Welch's correction the statistical comparison are: (***) pWT- virRmut = 4.1 10-4 with t = 6.1, df = 7.5, (**) p virRmut - virRmut-C = 0.007 with t = 3.2, df = 13.2, E) Using a two-tailed t test with Welch's correction the statistical comparison are: (****) pWT- virRmut = 6.6 10-10 with t = 16.3, df = 12.7, (**) p virRmut - virRmut -C = 0.01 with t = 3.0, df = 13.2., F) Using a two-tailed t test with Welch's correction the statistical comparison are: (****) pWT- virRmut = 2.8 10-18 with t = 17.8, df = 32.3, (****) virRmut - virRmut -C = 3.9 10-17 with t = 16.4, df = 31.8.

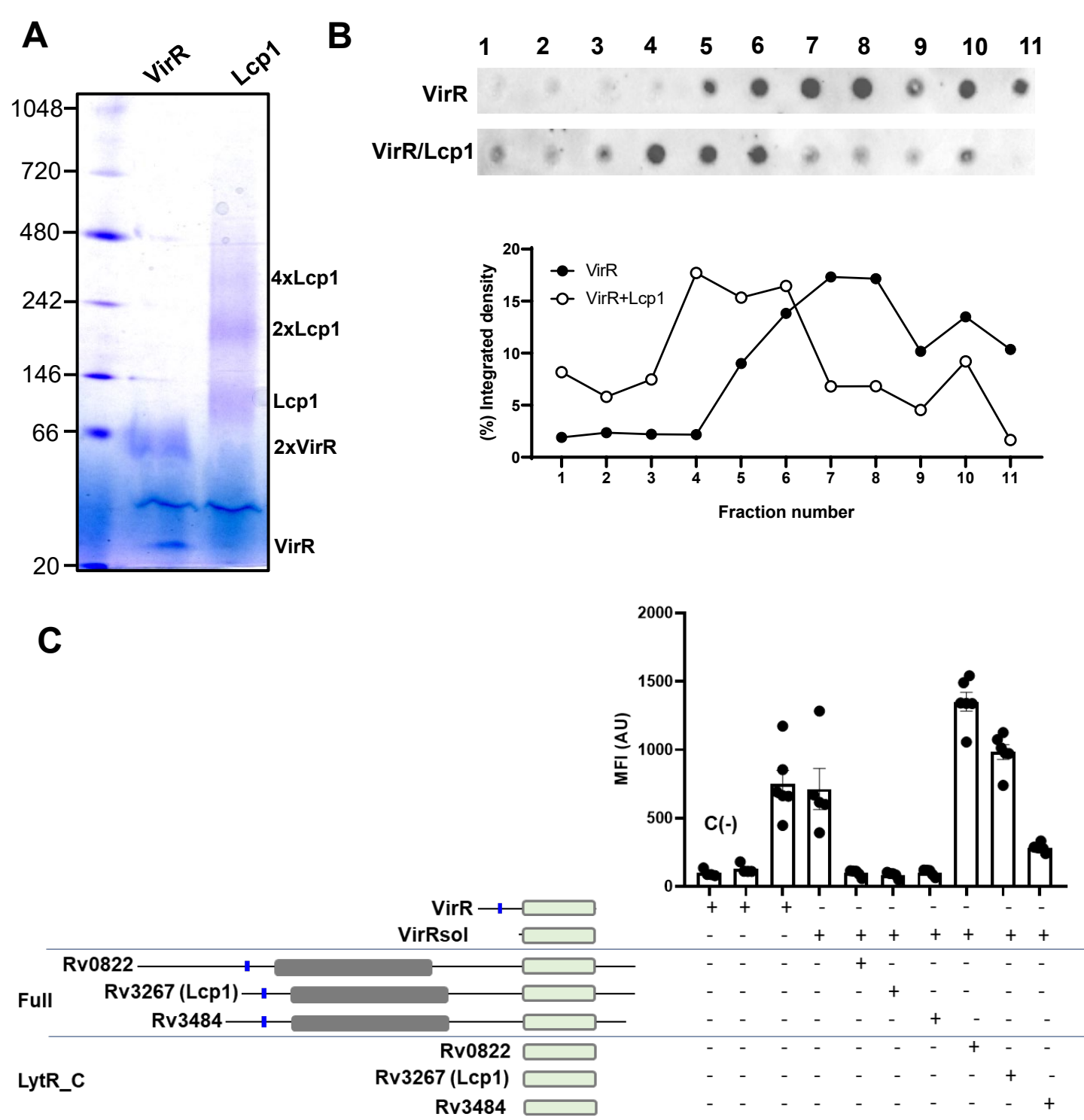
A
VirR
Lcp1
1048
720
480
242
146
66
20
4xLcp1
2xLcp1
Lcp1
2xVirR
VirR
B
1 2 3 4 5 6 7 8 9 10 11
VirR
VirR/Lcp1
(%) Integrated density
VirR
VirR+Lcp1
Fraction number
C
MFI (AU)
C(-)
VirR
VirRsol
Rv0822
Rv3267 (Lcp1)
Rv3484
Full
LytR_C

Figure 8

Figure 8. VirR interacts with Lcp1. (A) Blue-native PAGE analysis of recombinant VirR and Lcp1. The molecular mass of markers in kDa are indicated on the left side of the gel. The size of the multimers of VirR and Lcp1 are indicated on the left side of the gel. (B) Upper panel. Representative image of a flotation assay of recombinant VirR alone or in combination with Lcp1 performed on an idioxanol density gradient. The presence of VirR was detected in each fraction by dot-blot using murine polyclonal antibodies raised against VirR. Numbers indicate collected fractions from top (1) to bottom (11). Lower panel. Quantification of the dot-blot by measuring the pixel intensity of the dots using ImageJ. Data are mean and standard error of three independent experiments. (C) Bipartite split-GFP experiment using M. smegmatis D2 expressing plasmids depicted in (Fig S9A), including VirR, VirRsol(1-41), CtpCN, Rv3484, Rv3267 (Lcp1), Rv0822, Rv3484LytR_C, Rv3267LytR_C and Rv0822LytR_C. Bacteria were grown in complete 7H9. Fluorescence was recorded by epifluorescence microscopy. The experiment was performed one time.